



HAL
open science

Structural and Metamorphic History of the Leech River Shear Zone, Vancouver Island, British Columbia

C. Seyler, J. Kirkpatrick, C. Faber, Alexis Licht, D. Šilerová, C. Regalla

► **To cite this version:**

C. Seyler, J. Kirkpatrick, C. Faber, Alexis Licht, D. Šilerová, et al.. Structural and Metamorphic History of the Leech River Shear Zone, Vancouver Island, British Columbia. *Tectonics*, 2022, 41 (11), 10.1029/2021TC007132 . hal-03867718

HAL Id: hal-03867718

<https://hal.science/hal-03867718>

Submitted on 23 Nov 2022

HAL is a multi-disciplinary open access archive for the deposit and dissemination of scientific research documents, whether they are published or not. The documents may come from teaching and research institutions in France or abroad, or from public or private research centers.

L'archive ouverte pluridisciplinaire **HAL**, est destinée au dépôt et à la diffusion de documents scientifiques de niveau recherche, publiés ou non, émanant des établissements d'enseignement et de recherche français ou étrangers, des laboratoires publics ou privés.

1 **Structural and metamorphic history of the Leech River Shear Zone, Vancouver**
2 **Island, British Columbia**

3
4 **C. E. Seyler^{1†*}, J. D. Kirkpatrick¹, C. Faber², A. Licht^{3,4}, D. Šilerová^{1‡}, and C. Regalla⁵**

5 ¹Department of Earth and Planetary Sciences, McGill University, Montréal, QC, Canada

6 ²Department of Geosciences, UiT The Arctic University of Norway, Tromsø, Norway

7 ³Aix-Marseille Université, CNRS, Centre de Recherche et d'Enseignement de Géosciences de
8 l'Environnement (CEREGE), Aix-en-Provence, France

9 ⁴Department of Earth and Space Sciences, University of Washington, Seattle, WA, USA

10 ⁵School of Earth and Sustainability, Northern Arizona University, Flagstaff, AZ, USA

11 [†]Now at University of Texas Institute for Geophysics and Department of Geological Sciences,
12 University of Texas, Austin, TX, USA

13 [‡]Now at Department of Earth Sciences, Simon Fraser University, Burnaby, BC, Canada

14 * *Corresponding author:* Caroline Seyler (caroline.seyler@utexas.edu)

15
16 **Key Points**

- 17 • Leech River Shear Zone confirmed as a hot, Eocene-age paleo-subduction interface
- 18 • High-temperature metamorphism produced by ridge subduction during accretion of
- 19 Siletz-Crescent terrane
- 20 • New detrital zircon ages from the Leech River Schist support near-trench deposition
- 21 during Paleocene

22
23 **Abstract**

24 The Leech River Shear Zone (LRSZ) on southern Vancouver Island separates the

25 metasedimentary schists of the Leech River Complex from the accreted oceanic plateau of the

26 Siletz-Crescent terrane. The juxtaposition of these rock units suggests a possible origin as a

27 subduction plate boundary, but tectonic context of the LRSZ has yet to be fully established. We
28 present field, microstructural, petrological, and geochronological observations that constrain the
29 structural and metamorphic history of LRSZ. The mylonite zone of the LRSZ straddles the
30 lithologic contact between the schists of the Leech River Complex and basalts of the Siletz-
31 Crescent terrane. Foliation orientations, a steeply plunging stretching lineation, and kinematic
32 indicators all suggest reverse-sinistral motion. Compositions of garnet in the schist and
33 amphibole in the metabasalt record syn-kinematic growth at temperature and pressure conditions
34 of 550–570 °C and 450–490 MPa. These metamorphic conditions require elevated geotherms
35 that are consistent with plate models that position the Kula-Farallon Ridge and Yellowstone
36 Hotspot in the region in the Eocene (~50 Ma). Detrital zircon U-Pb age distributions for the
37 Leech River Schist have Paleocene maximum depositional ages and are similar to the Upper
38 Nanaimo Group that unconformably overlies the Wrangellia terrane. Our ages support early
39 Paleocene deposition of the schist in a subduction trench/slope environment followed by
40 underthrusting and underplating. These results establish the exhumed mylonite zone of the LRSZ
41 as a paleo-plate interface that was active during Eocene subduction.

42 **1 Introduction**

43 Subduction zone dynamics are strongly influenced by the mechanical properties of subduction
44 interface shear zones (Behr et al., 2022). However, the relevant properties of subduction
45 interfaces, such as their widths, rock types, and internal structure, cannot be determined via
46 geophysical observation. Instead, field- and micro-scale observations of exhumed shear zones
47 that were active during subduction are needed to fill this knowledge gap. Subduction dynamics
48 and thermal gradients evolve as they mature (e.g., Holt & Condit, 2021), and subduction zones
49 can encompass a broad range of environments (Chelle-Michou et al., 2022), for example, when
50 influenced by atypical subduction geometries like ridge subduction (e.g., DeLong et al., 1979;
51 Sakaguchi, 1996; Brown, 1998). A more complete inventory capturing the variability of
52 subduction interfaces is therefore needed to better understand their behavior.

53

54 The Canadian Cordillera potentially exposes numerous subduction-related structures as it was
55 assembled through a series of accretionary orogenies. One candidate structure is the Leech River
56 Fault (Fig. 1), a terrane-bounding fault located on southern Vancouver Island in British

57 Columbia that juxtaposes mafic volcanic and igneous rocks of the Metchosin Igneous Complex
58 (MIC) to the south with the predominantly metapelitic Leech River Complex (LRC). For clarity,
59 we will term this structure the “Leech River Shear Zone” (LRSZ) to differentiate it from the
60 recently active “Leech River Fault”, which is locally coincident (Morrell et al., 2017, 2018; Li et
61 al., 2018; Harrichhausen et al., 2021). The MIC is part of the Siletz-Crescent terrane, a ~10–30
62 km-thick sequence of Eocene mafic volcanics and intrusive suites that extends from Vancouver
63 Island to Oregon. Trace element and rare earth element geochemistry of basalts from the terrane
64 (Phillips et al., 2017), combined with the terrane’s thickness (Clowes et al., 1987; Tréhu et al.,
65 1994), indicate the Siletz-Crescent terrane represents a portion of a large igneous province that
66 formed on the Farallon plate, near the Kula/Resurrection-Farallon ridge, and above a mantle
67 plume, potentially the Yellowstone Hotspot (Wells et al., 2014; Phillips et al., 2017). Accretion
68 of the Siletz-Crescent terrane is therefore inferred to have occurred during subduction and
69 impacted the deformation of the subduction forearc and tectonics of the upper plate (Eddy et al.,
70 2016).

71
72 Previous work on the LRSZ presents conflicting interpretations of the tectonic context of this
73 structure. Seismic reflection images show the contact between the LRC and MIC extends from
74 the surface trace of the LRSZ, and dips to the north under Vancouver Island and projects to the
75 surface trace of the LRSZ (Clowes et al., 1987; Matharu et al., 2014). Combined with the ages of
76 the LRC (Cretaceous; Groome et al., 2003) and MIC (Eocene; Duncan, 1982; McCrory &
77 Wilson, 2013), this geometry suggests the LRSZ hosted reverse-sense motion, consistent with
78 formation in a subduction setting. However, previous field data suggests dominantly strike-slip
79 motion (Fairchild & Cowan, 1982; Groome, 2000), possibly related to development of a forearc
80 rift basin formed on the continental margin, which was previously proposed as the tectonic origin
81 of the MIC (Babcock et al., 1992; Wells et al., 1984). The origin of the LRC is also uncertain due
82 to the lack of a depositional age and its previous interpretation as allochthonous to Vancouver
83 Island (Fairchild & Cowan, 1982).

84
85 In this study, we use structural, petrological, and geochronological data to re-evaluate the
86 tectonic origin of the LRSZ and the LRC. We directly tested the thrust vs. strike-slip faulting
87 regime with field and microstructural observations that establish the kinematics of deformation.

88 We probed mineral compositions (garnet and amphibole), applied the Ti-in-biotite
89 geothermometer, and conducted phase equilibrium modeling to develop metamorphic histories
90 for the shear zone rocks and determine the syn-kinematic P-T conditions. We also measured the
91 U-Pb dates of detrital zircons from the LRC to determine its depositional age and setting. Our
92 results provide the first constraints on the paleogeographic and tectonic origin of the LRC and
93 the syn-kinematic pressure, temperature, and timing of deformation on the LRSZ. The results
94 indicate that the LRSZ was an Eocene-age, hot subduction interface that formed during
95 underthrusting of the Siletz-Crescent terrane beneath the previously underplated LRC as the
96 Farallon plate subducted under North America.

97 **2 Geologic setting**

98 The LRSZ is an east-west trending, terrane-bounding structure that separates the Leech River
99 Complex (LRC) north of the fault from the Metchosin Igneous Complex (MIC) to the south. The
100 LRC, together with the Pandora Peak Unit and Pacific Rim Complex, collectively make up the
101 Pacific Rim terrane, a southern correlative of the Chugach-Prince William accretionary
102 complexes in Alaska (Cowan, 2003; Cowan et al., 1997; Garver & Davidson, 2015). The MIC,
103 the Crescent Formation of Washington, the Coast Range Volcanic Province of Washington and
104 Oregon, and the Siletz River Volcanics of Oregon comprise the Siletz-Crescent terrane (Duncan,
105 1982; Irving, 1979; McCrory & Wilson, 2013; Simpson & Cox, 1977).

106 *2.1 Leech River Shear Zone*

107 The LRSZ has been previously reported as a fault zone with two to four discrete left-lateral strike
108 slip faults, lacking any fault gouge, breccia, or mylonitization (Fairchild & Cowan, 1982) as well
109 as a left-lateral shear zone composed of mylonites ("Bear Creek Shear Zone" in Groome, 2000).
110 The interpretation of the LRSZ as a left-lateral strike slip fault was largely based on the regional
111 steep dip of the fault (Fairchild & Cowan, 1982). Limited observations of shear sense indicators
112 from mylonites within the Bear Creek Shear Zone indicate left-lateral motion (Groome, 2000).
113 Quaternary reactivation of this structure as a wide zone of strike-slip faults has been documented
114 through identification of fault scarps (Morell et al., 2017), microseismicity (Li et al., 2018), and
115 paleoseismic trenching (Morell et al., 2018; Harrichhausen et al., 2021). Here, we focus on the
116 ancient structure that established the tectonic contact between the LRC and MIC (the "Leech

117 River Shear Zone”), rather than the recently active “Leech River Fault”, which is locally parallel
118 and co-located with the terrane boundary and mylonite zone of the LRSZ

119 *2.2 Leech River Complex*

120 The LRC is an approximately 10 km-thick package of metasedimentary rocks that crop out in an
121 east-west trending unit on southern Vancouver Island (Fig. 1). The LRC is bounded to the north
122 by the San Juan and Survey Mountain faults, which juxtapose the LRC with the Wrangellia
123 terrane and the Pandora Peak Unit of the Pacific Rim terrane, respectively (Rusmore & Cowan,
124 1985). The LRC includes the Leech River Schist (LRS), the Jordan River Unit, the Tripp Creek
125 Metabasite, and the Walker Creek intrusions (Fairchild & Cowan, 1982).

126

127 The LRS is a metapelitic schist containing metapsammitic layers. Based on the assemblage of
128 discontinuous layers of metamorphosed shales and sandstones with minor chert and basaltic
129 volcanics, the LRS was interpreted as a submarine, near-continental margin turbidite sequence
130 deposited near a source of basalt, such as a spreading ridge (Fairchild & Cowan, 1982; Muller,
131 1977b, 1980). The LRS has a reported maximum depositional age of 103 Ma derived from the
132 youngest detrital zircon dated by Groome et al. (2003). Fairchild and Cowan (1982) reported
133 transposed sedimentary layering, aligned metapsammitic lenses within a metapelitic matrix, and
134 two generations of folds with strong axial planar foliation parallel to the compositional layering.
135 These features were interpreted to result from regional north-south shortening (Fairchild &
136 Cowan, 1982). The metamorphic grade of the LRS increases from greenschist facies in the north
137 (chlorite-white mica-biotite phyllites), to amphibolite facies in the south (garnet-staurolite-
138 andalusite schists), and metamorphism was syn- to post-kinematic with regional deformation
139 (Fairchild & Cowan, 1982; Rusmore & Cowan, 1985; Groome et al., 2003). Previous work
140 indicated that the metamorphic gradient was isobaric based on the progression of metamorphic
141 assemblages through a series of east-west isograds for biotite, garnet, staurolite, and andalusite
142 (Rusmore & Cowan, 1985). Estimates of peak pressure (< 350 MPa) and temperature (500–600
143 °C) are attributed to the presence of andalusite in the southern region within contact aureoles
144 around intrusive units (Rusmore, 1982; Groome et al., 2003).

145

146 The Jordan River Unit is a quartz-feldspar-biotite schist that has been interpreted as both the
147 largest body of metasandstone in the LRS (i.e., the Valentine metasandstone in Fairchild &
148 Cowan, 1982; Muller, 1980), and as a plagioclase-rich peraluminous metagranodiorite intrusion
149 derived from anatexis of the LRS with a titanite U-Pb crystallization age of 88 Ma (Groome et
150 al., 2003). The Tripp Creek Metabasite is an actinolite-plagioclase-quartz-garnet schist
151 interpreted as an intrusive unit due to the presence of foliated LRS xenoliths (Groome et al.,
152 2003). The Jordan River Unit and Tripp Creek Metabasite have a schistosity parallel to the
153 foliation in the LRS, suggesting their formation is pre- to syn-kinematic with deformation of the
154 complex. The Walker Creek intrusions are a suite of tonalite, trondhjemite, and granodiorite
155 dikes and sills present in the southern portion of the LRS. Deformation of these intrusions is non-
156 uniform, with some dikes displaying schistosity parallel to the foliation in the LRS while others
157 remain undeformed, suggesting syn- to post-kinematic magmatism (Groome et al., 2003). These
158 intrusions have zircon U-Pb crystallization ages ranging from 51-47 Ma, and their geochemical
159 signatures suggest they are derived from anatexis of the LRS (Groome et al., 2003).

160 *2.3 Metchosin Igneous Complex*

161 The MIC consists of a 3 km-thick ophiolitic pseudostratigraphy consisting of gabbro stocks
162 (Sooke Gabbros), sheeted dikes, and a sequence of basalt flows that transitions from submarine
163 to subaerial up-section (Massey, 1986). Whole rock trace element geochemistry is transitional
164 between N-MORB and E-MORB signatures, suggesting both spreading ridge- and mantle
165 plume- related magmatism (Duncan, 1982; Phillips et al., 2017; Timpa et al., 2005). The age of
166 the complex ranges from 58–52 Ma based on $^{40}\text{Ar}/^{39}\text{Ar}$ fusion dates and U-Pb zircon dates
167 (Duncan, 1982; Massey, 1986; Yorath et al., 1999). Temperature estimates from amphibole
168 compositions and Al^{iv} -in-chlorite geothermometry suggest the metamorphic grade in the
169 complex increases from prehnite-actinolite in the east to amphibolite in the west along a ~5–10
170 °C/km horizontal gradient (Timpa et al., 2005). This gradient was interpreted as the result of
171 metamorphism during tectonic emplacement of the MIC followed by differential exhumation
172 (Timpa et al., 2005).

173

174 Two contrasting origins for the Siletz-Crescent terrane have been proposed: an oceanic plateau
175 (originally proposed by Duncan (1982)), or extensional volcanism in a forearc rift (Babcock et

176 al., 1992; Wells et al., 1984). However, the revised 55–49 Ma age range for the terrane (Eddy et
177 al., 2017; McCrory & Wilson, 2013; Wells et al., 2014 and references therein), plate
178 reconstruction modeling (McCrory & Wilson, 2013; Wells et al., 2014), and basalt geochemistry
179 (Phillips et al., 2017) suggest that the Siletz-Crescent terrane represents an accreted oceanic
180 plateau that formed near the Kula/Resurrection-Farallon Ridge by a near-ridge mantle plume,
181 most likely the Yellowstone Hotspot (Duncan, 1982; Eddy et al., 2016; Eddy et al., 2017;
182 McCrory & Wilson, 2013; Phillips et al., 2017; Wells et al., 2014). Shortly after its formation,
183 the Washington and Oregon portion of the terrane docked to North America by 51–48 Ma based
184 on the coccolithophores present in the overlying strata (Wells et al., 2014), the sedimentary
185 record of changing paleoflow direction (Eddy et al., 2016), and the age of intrusives (Eddy et al.,
186 2017). On Vancouver Island, the terrane docked prior to 45–42.5 Ma based on $^{40}\text{Ar}/^{39}\text{Ar}$ cooling
187 ages in mica that record exhumation of the Leech River Schist (Groome et al., 2003), which is
188 inferred to have been due to uplift related to MIC underplating.

189 **3 Methods**

190 *3.1 Detrital zircon analysis*

191 Detrital zircon ages were determined for samples of the Leech River Schist, Jordan River Unit,
192 and Walker Creek intrusions (sample locations in Table S1). Detailed data acquisition and
193 reduction protocols are described in Shekut and Licht (2020). Zircons were extracted by heavy
194 mineral separation, including concentration with a Holman-Wilfley™ gravity table, density
195 separation with methylene iodide, and magnetic separation with a Frantz™ Magnetic Barrier
196 separator. Data was collected using a laser-ablation inductively-coupled-plasma mass-
197 spectrometry (LA-ICP-MS), using an iCAP-RQ Quadrupole ICP-MS coupled to an Analyte G2
198 excimer laser at the University of Washington, using a spot diameter of 25 microns and
199 Plešovice zircons as calibration reference material (Sláma et al., 2008). Data reduction was
200 conducted with *Iolite* (Version 3.5), using their *U_Pb_Geochron4* Data Reduction Scheme to
201 calculate U-Pb dates uncorrected for common lead (Paton et al., 2010). Uncertainties for all
202 samples were calculated using a modified version of the method of Matthews and Guest (2017)
203 that takes into account the impact of ^{207}Pb beam intensity on date uncertainties (Horstwood et al.,
204 2016). The dates used for plotting are $^{206}\text{Pb}/^{238}\text{U}$ for dates <1400 Ma and $^{207}\text{Pb}/^{206}\text{Pb}$ for dates
205 >1400 Ma. Dates >300 Ma were screened for concordance using a discordance filter at >20%

206 discordance (<80% concordance) and >5% reverse discordance (>105% concordance); we used
207 the $^{206}\text{Pb}/^{238}\text{U}$ vs $^{207}\text{Pb}/^{235}\text{U}$ ratio to calculate discordance for dates <1300 Ma, and the $^{206}\text{Pb}/^{238}\text{U}$
208 vs. $^{207}\text{Pb}/^{206}\text{Pb}$ ratio for older dates. A subset of zircon grains from each sample were imaged
209 using cathodoluminescence to assess their growth textures (Fig. S1). Maximum depositional ages
210 (MDA) were calculated from the youngest age population of overlapping dates ($n \geq 3$) using the
211 *TuffZirc* application within IsoPlot (Ludwig, 2003).

212 *3.2 Mineral composition analysis*

213 Electron probe micro-analysis (EPMA) was conducted on representative thin sections of the
214 schist and metabasalt mylonites from the LRSZ to determine the syn-kinematic P-T conditions.
215 Polished thin sections were prepared perpendicular to the foliation and parallel or perpendicular
216 to the lineation from oriented samples (Table S1). Mineral compositions were measured with 5
217 wavelength-dispersive spectrometers on either a JEOL 8900 electron microprobe or Cameca
218 SX100 Five-FE electron microprobe. Garnet compositions were measured on a Cameca
219 microprobe with an accelerating voltage of 15 kV, a beam current of 20 nA, and a beam diameter
220 of 5 μm . Biotite compositions from samples CS15-DR21 and CS15-SW06 were measured on a
221 JEOL microprobe with an accelerating voltage of 15 kV, a beam current of 20 nA, and a beam
222 diameter = 10 μm . Biotite from samples CS18-25 and CS18-32 were measured on a Cameca
223 microprobe with an accelerating voltage of 15 kV, a beam current of 20 nA, and a beam diameter
224 of 5 μm . Amphibole compositions were measured on a Cameca microprobe with an accelerating
225 voltage of 20 kV, a beam current of 4 nA, and a beam diameter of 5 μm . Amphibole
226 compositions were calculated based on the recommendations and classification scheme approved
227 by the Commission on New Minerals Nomenclature and Classification (CNMNC) of the
228 International Mineralogical Association (Hawthorne et al., 2012; Locock, 2014). Plagioclase
229 compositions were measured on a Cameca microprobe with an accelerating voltage of 15 kV, a
230 beam current of 20 nA, and a beam diameter of 5 μm . Bulk rock compositions were determined
231 by Actlabs using whole rock fusion X-ray fluorescence (XRF) analysis. Phase equilibrium
232 modeling was conducted with *PerpleX* software (version 6.9.9; Connolly, 2005) using the
233 internally consistent dataset of Holland and Powell (1998, revised 2004).

234 **4 Field observations of the hanging wall and footwall**

235 In this section, we describe the LRS to the north and MIC to the south to differentiate the
236 deformation associated with the shear zone from regional structures. Our study area extends from
237 the western coast of the island to the Diversion and Bear Creek reservoirs (Fig. 1). Exposures are
238 best along the coast, in road cuts along Highway 14 and logging roads north of the reservoirs,
239 and around the shores of the reservoirs. Elsewhere, the exposure is very poor due to dense
240 vegetation and till cover. Targeted field sites include Botany Bay (LRS), north of the reservoirs
241 (LRS), and Sombrio Point (Metchosin Basalt).

242 *4.1 Leech River Schist (hanging wall of the LRSZ)*

243 The structural fabrics and metamorphic grade of the Leech River Schist vary throughout the unit.
244 We describe the schist in two localities to illustrate this variability: a ~0.5 km² area around
245 Botany Bay located ~5 km north of the mapped trace of the LRSZ (projected offshore), and
246 north of the Diversion and Bear Creek reservoirs, a transect from the northern edge of the high
247 strain zone up to ~2 km north of the LRSZ.

248
249 At Botany Bay, the schist is characterized by a block-in-matrix fabric with quartz- and
250 plagioclase-rich metapsammitic blocks hosted in a phyllosilicate-rich metapelitic matrix (Fig.
251 2a–d). Some larger blocks contain evidence for graded bedding and crossbeds indicating that the
252 lithologic variation represents primary sedimentary bedding (S_0), which included interbedded
253 sand-, silt-, and clay-sized layers. The present-day layer discontinuity and strong deformation
254 fabrics in the matrix, including solution cleavage, imply that bedding was tectonically disrupted
255 and transposed into the block-in-matrix fabric. Block sizes range from centimeter- to meter-scale
256 and larger blocks commonly contain quartz veins that terminate at the block edges. Two foliation
257 orientations are present, with the dominant foliation (S_1) defined by parallel long axes of blocks
258 forming an apparent layering that is parallel to a continuous cleavage in the metapelitic matrix. A
259 less pronounced, spaced cleavage (S_2) in the metapelitic matrix is discordant to the S_1 cleavage
260 (Fig. 2a). Both S_1 and S_2 strike approximately east-west, but S_2 is more steeply dipping, resulting
261 in an intersection lineation that plunges shallowly to the west (Fig. 1c and 3a). Some quartz veins
262 within the blocks are tightly folded with axial surfaces parallel to the S_1 foliation. Asymmetric
263 isoclinal folds of thin metapsammitic blocks intrafolial with S_1 are also observed, which indicate

264 that S_0 is transposed into S_1 (Fig. 2b). The S_2 foliation is axial planar to tight, asymmetric,
265 disharmonic folding of the S_1 foliation, which exhibits a top-to-the-south vergence direction (Fig.
266 2c). Later quartz veins crosscut both the blocks and matrix at a low angle to S_1 foliation and are
267 moderately deformed into the S_1 foliation (Fig. 2d). The S_2 foliation is defined by white mica and
268 chlorite, indicating deformation at greenschist conditions (Rusmore, 1982).

269
270 North of the Diversion and Bear Creek reservoirs, the schist is characterized by disordered and
271 discontinuous deformation fabrics rather than a block-in-matrix structure (Fig. 2e). The dominant
272 foliation is defined by dismembered compositional layering of metapsammitic and metapelitic
273 layers (millimeters to 2–3 cm-thick), which is transposed and locally parallel to a grain shape
274 preferred orientation of phyllosilicate minerals in the phyllitic layers. The compositional layering
275 is transposed, with an axial planar cleavage. This composite foliation is wavy and irregular,
276 strikes roughly east-west, and dips steeply to the north (Fig. 1d). Asymmetric, tight folds of the
277 layering with parasitic folding are common in both subhorizontal or subvertical sections with
278 top-to-the-west and top-to-the-south vergence, respectively. The similar attitudes of the dominant
279 foliation in this region to the S_2 foliation near Botany Bay, along with the similar vergence
280 direction of asymmetric folds, suggests foliations formed under the same shortening direction.
281 We interpret the dominant foliation north of the reservoirs as an S_2 foliation that has transposed
282 and folded the S_0 - S_1 foliation (cf. Fairchild & Cowan, 1982). Quartz veins crosscut the foliation
283 at low and high angles and are often boudinaged and folded with the foliation. Coarse-grained
284 (~1-10 mm) metamorphic minerals of garnet, biotite, staurolite, and andalusite are sometimes
285 present in outcrop, indicating amphibolite grade metamorphism. The foliation is deflected
286 around these grains, suggesting porphyroblast growth was pre- and/or syn-kinematic. Overall,
287 the highly dismembered compositional layers, smaller scale of quartz-plagioclase boudins, and
288 transposition of the S_1 foliation to parallel with S_2 suggests that this region is relatively higher
289 strain compared to the schist at Botany Bay.

290

291 *4.1.1 Detrital zircon U-Pb*

292 We investigated the origin of the Leech River Complex with detrital zircon geochronology to re-
293 evaluate its depositional age and help determine if the Jordan River Unit is metasedimentary or
294 intrusive. U-Pb ages were analyzed from zircon grains in four samples (sample locations in Fig.

295 1a): one sample of Walker Creek intrusions, one sample of Leech River Schist, and two samples
296 of the Jordan River Unit, which has been inconsistently described as either a metasediment
297 (Fairchild & Cowan, 1982; Muller, 1980) or an igneous intrusion (Groome et al., 2003).

298

299 The MDA of the Leech River Schist sample is 64.4 ± 2.4 (2σ) Ma and the MDA of the Jordan
300 River samples are 66.9 ± 2.1 Ma and 61.0 ± 2.3 Ma (2σ) (Fig. 3a; Table S3). Zircons in the Leech
301 River Schist and Jordan River metasediment are detrital, with two significant peaks at 60–100
302 Ma and 140–200 Ma and a cluster of minor peaks between 1100–1800 Ma. Mesozoic zircons
303 were likely sourced from the nearby Coast Mountains Batholith, the volcanic arc formed from
304 Jurassic-Cretaceous subduction beneath the western margin of Wrangellia (Cecil et al., 2018;
305 Friedman & Armstrong, 1995; Gehrels et al., 2009). Precambrian zircons have several possible
306 sources, which are discussed below. The similar U-Pb age distribution and MDAs for the Leech
307 River Schist and Jordan River Unit, together with petrographic observations (Fig. S2), support
308 the interpretation that the Jordan River Unit is metasedimentary (as defined by Fairchild and
309 Cowan (1982) and Muller (1980)). The Walker Creek intrusion contains very few zircons. The
310 youngest zircon age in the Walker Creek sample is 47.5 ± 1.6 Ma (2σ), which may represent a
311 crystallization age, but this is inconclusive. The Walker Creek age distribution matches
312 distributions from the Leech River Schist and Jordan River metasediment, suggesting these
313 zircons were all inherited during *in situ* partial melting of the schist, consistent with the
314 peraluminous compositions of the intrusions.

315 4.2 Metchosin Basalt (footwall of the LRSZ)

316 The Metchosin Basalt is a very fine-grained to aphanitic amygdaloidal basalt composed of
317 pyroxene or amphibole + plagioclase + epidote + titanite \pm chlorite \pm quartz. Near Sombrio
318 Point, south of the shear zone, the basalt is massive with preserved volcanic textures, including
319 several meters-scale pillows which contain amygdules. Pillows and pillow interstices contain
320 patches of epidote-rich rock as well as abundant epidote veins (Fig. 2f). There is no grain-scale
321 or distributed foliation, so there is little evidence of pervasive deformation, but small faults with
322 no preferred orientation are observed locally. The lack of consistent deformation fabrics in the
323 basalt away from the LRSZ suggest that the basalt has experienced negligible distributed internal
324 deformation.

325 **5 Field and microstructural observations of the Leech River Shear Zone**

326 In this section, we describe the structure, kinematics, and metamorphism of the LRSZ. Our study
327 area is focused on 10s m² exposures predominantly located around the Diversion and Bear Creek
328 reservoirs (Fig. 1), with other exposures located in a region ~12 km along strike toward the
329 coast.

330 *5.1 Structure and kinematics*

331 The LRSZ is an approximately 600-m wide mylonitic shear zone that deformed both the Leech
332 River Schist and the Metchosin Basalt. We define the LRSZ as a high strain zone that contains
333 distinct mylonitic fabrics and kinematic indicators compared to the surrounding rocks. In the
334 schist, the shear zone is characterized by planar and composite foliations, abundant deformed
335 quartz veins, isoclinal folds with subhorizontal and steeply plunging fold axes, and a reduction in
336 grain size (notably of porphyroblasts). In the metabasalt, the shear zone is characterized by
337 planar foliation development and the presence of metamorphic amphibole. The edges of the
338 LRSZ in both lithologies are gradational, and the mylonite zone is wider in the schist than in the
339 metabasalt. The large-scale architecture of the shear zone, including potential lithologic mixing
340 and deformation heterogeneity, is not well constrained due to limited exposure. A lithologic
341 contact between the schist and metabasalt mylonites was only observed in the spillway between
342 the reservoirs, where the contact is sharp and planar over the extent of the outcrop, which is ~10
343 m in length along strike.

344

345 The Leech River Schist mylonite is a strongly foliated and lineated, fine-grained rock (Fig. 4a–
346 e). The mylonitic foliation is sub-parallel to the map-scale structure, striking approximately east-
347 west and dipping steeply (average ~70°) to the north (Fig. 1e). This foliation is defined by
348 subparallel compositional layers, a composite S-C-C' foliation within phyllosilicate-rich layers,
349 and a ubiquitous grain shape preferred orientation that is locally parallel to the compositional
350 layers (Fig. 1e, 4a–d, and 5a,b). Elongate grains and aggregates of aligned phyllosilicates on
351 foliation planes define a penetrative, steeply plunging stretching lineation (Fig. 1e and 4e).
352 Compositional layers (millimeters to centimeters thick with rare ~10s cm-thick layers) are
353 differentiated by changes in the relative proportion of phyllosilicates, quartz, and feldspar,
354 equivalent to the layering between metapsammitic and metapelitic lithologies north of the shear

355 zone. These layers are typically planar and continuous for up to tens of centimeters to meters,
356 with lengths limited by boudinage or exposure, such that the layering is extremely attenuated
357 relative to outside the shear zone. Three types of folds affect the layering within the schist
358 mylonite (Fig. 1e). Isoclinal folds of the layering have axial planes parallel to the mylonitic
359 foliation and both sub-horizontal and steeply plunging hinges (Fig. 4b,c). Tight folds of the
360 layering are less common and have axial planes at a low angle to the foliation and steeply
361 plunging axes subparallel to the stretching lineation (Fig. 4f). Kink folds of the foliation are rare
362 and have axial planes at a high angle to the foliation (Fig. 4f). Asymmetry exhibited by all fold
363 types is generally consistent with north-side up reverse shear in subvertical exposures and left-
364 lateral shear in subhorizontal exposures. Shear bands that deflect the layering, boudin margins,
365 and quartz veins define the C-C' composite foliation. We interpret the mylonitic foliation (S_3) to
366 be axial planar to isoclinal folds of S_{0-2} , which are all parallel due to transposition within the
367 shear zone.

368
369 The Metchosin metabasalt mylonite contains a strong foliation defined by millimeter- to
370 centimeter-scale compositional layering between plagioclase- and amphibole-rich layers (Fig. 1e
371 and 4g,h). Some compositional layers are boudinaged with boudin long axes parallel to the
372 layering. At the grain-scale, large (~200–500 μm) asymmetric amphibole porphyroblasts are
373 surrounded by a fine-grained amphibole, plagioclase, and sometimes epidote matrix (Fig. 6).
374 Amphibole, plagioclase ribbons, and subparallel trains of titanite and ilmenite grains all show
375 shape-preferred orientations parallel to the compositional layering. Subparallel long axes of
376 amphibole minerals define a steeply plunging, penetrative mineral lineation in the metabasalt
377 mylonite (Fig. 1e).

378
379 Quartz veins centimeters to tens of meters long are present in both the schist and metabasalt,
380 though they are far more abundant in the schist mylonite. The range of shapes and attitudes of
381 the veins indicates they were progressively deformed during noncoaxial deformation. Most veins
382 are boudinaged into asymmetric shapes or are isoclinally folded with asymmetric geometries,
383 with axial planes subparallel to the mylonitic foliation and steeply plunging hinges (Fig. 1e and
384 4). A few veins exhibit folded axial surfaces, indicating they were re-folded and likely formed
385 relatively early in the deformation history. The latest veins are planar and crosscut the foliation at

386 apparent angles of $\sim 30^\circ$ in subhorizontal exposures. Large sets of sheeted veins are tens of
 387 centimeters to around one meter thick and can be traced for hundreds of meters along strike (Fig.
 388 4a). These sheeted veins are present in both the schist and metabasalt mylonites and contain
 389 centimeter-thick layers of quartz separated by sub-millimeter layers of phyllosilicates or
 390 amphibole, respectively, interpreted as selvages of the local wall rock. They are also isoclinally
 391 folded with steeply dipping axial surfaces subparallel to the mylonitic foliation and are
 392 occasionally boudinaged.

393

394 Kinematic indicators observed in outcrop (Fig. 4) and in thin section (Fig. 5 and 6) in both the
 395 schist and metabasalt mylonites exhibit north-side-up reverse-sense kinematics in steeply dipping
 396 exposures and sections (i.e., perpendicular to the foliation and containing the lineation) and
 397 apparent sinistral kinematics when viewed in subhorizontal exposures (i.e., perpendicular to the
 398 lineation), with reverse-sense indicators most strongly expressed. Overall, the dominant reverse-
 399 sense indicators and steeply plunging lineation indicate predominantly thrust motion and
 400 secondary sinistral strike-slip motion, which is consistent with sinistral-oblique underthrusting of
 401 the Metchosin Basalt beneath the Leech River Schist.

402 *5.2 Pressure and temperature of deformation*

403 Pre- and syn-kinematic P-T conditions were determined with a combination of microstructural
 404 observations, mineral chemistry analyses, and phase equilibrium modeling. The schist mylonites
 405 in the LRSZ contain garnet + biotite + chlorite + muscovite + plagioclase + quartz + ilmenite \pm
 406 rutile \pm staurolite \pm andalusite \pm graphite (Fig. 5). Compositional layering between millimeter- to
 407 centimeter-thick quartz-plagioclase-rich, and phyllosilicate-rich layers dominates the
 408 microstructure (Fig. 5a) with porphyroblasts of garnet, staurolite, and andalusite. Quartz grains
 409 exhibit interlobate grain boundaries and subgrain development indicative of crystal-plastic
 410 deformation via dislocation creep (Fig. 5b). Garnet occurs within phyllosilicate-rich layers.
 411 Garnet porphyroblasts are euhedral, lack evidence of retrogression, and often have weakly
 412 asymmetric tails and pressure shadows of quartz and phyllosilicates in both lineation-parallel and
 413 lineation-perpendicular orientation (Fig. 5c,d). Some garnet grains are inclusion-free, while
 414 others have ilmenite and/or quartz inclusions. Ilmenite grains are also dispersed within mica-
 415 dominated layers in the matrix and are aligned with their long axes parallel to foliation. Fine-
 416 grained rutile is also present and occurs as elongate grains parallel to the foliation. Andalusite

417 porphyroblasts (~1–10 mm long) are fragmented, surrounded by reaction rims composed of
 418 muscovite and biotite, and have weakly asymmetric tails composed of chlorite, biotite, and
 419 muscovite (Fig. 5e). Staurolite porphyroblasts are partially replaced by chlorite and quartz and
 420 also have weakly asymmetric tails (Fig. 5f). Biotite porphyroblasts with their basal plane at an
 421 angle to the foliation are coarse-grained (~100–1000s μm long), blocky, and often contain
 422 graphite interlayers (Fig. 5g). Fine-grained biotite, chlorite, and muscovite are intergrown in
 423 phyllosilicate-rich layers with basal planes locally parallel to the foliation. These phyllosilicate-
 424 rich layers have variable proportions of each phase, and muscovite-chlorite layers are most
 425 common. The reaction rims around andalusite and staurolite porphyroblasts indicate
 426 disequilibrium with the matrix phases, and they are therefore likely pre-kinematic with respect to
 427 S_3 . Some samples show snowball garnets, indicating that garnet, at least partially, grew syn-
 428 kinematically with S_3 (Fig. 5d).

429

430 Garnet compositions were analyzed to establish the timing of garnet growth and define P-T
 431 conditions of metamorphism. Grain transects and compositional maps show zoning in all four
 432 garnet components (Fig. 7 and S3; Table S4). Spessartine content is at maximum in the cores
 433 (Sps_{26}) and decreases continuously through the mantles to a minimum of Sps_{15} in the rims,
 434 typical of prograde growth. Almandine content increases continuously from Alm_{58} in the cores
 435 up to Alm_{69} in the rims. Both pyrope and grossular contents show a continuous zonation profile
 436 through the cores and mantles, with compositions of $\text{Py}_{7.5}\text{Grs}_6$ with X_{Mg} at 0.11 in the cores to
 437 $\text{Py}_{10}\text{Grs}_4$ and X_{Mg} at 0.13–0.14 in the mantles. Both of these components then show a sharp
 438 decrease or increase, respectively, in a thin, asymmetric rim, which can be observed most clearly
 439 in the Ca map. The composition of this rim is around $\text{Alm}_{69}\text{Py}_9\text{Grs}_6\text{Sps}_{15}$ with an X_{Mg} of 0.12–
 440 0.13. The Ca map also shows growth zoning between the cores and mantles, however the
 441 continuity from cores through mantles in the other maps indicates that some diffusion has likely
 442 contributed to smoothing the profiles. The thin rims are asymmetric with respect to the S_3
 443 foliation, which indicates syn- S_3 growth of the rims. Garnet cores are therefore likely related to
 444 pre- S_3 metamorphism and rims related to shear zone deformation.

445

446 Based on the mineral textures and garnet zoning, two mineral assemblages can be defined for
 447 determination of a P-T path; a pre- S_3 assemblage includes garnet (cores) + ilmenite + quartz \pm

448 andalusite ± staurolite, and a syn-S₃ assemblage of garnet (rims) + biotite + chlorite + muscovite
 449 + quartz + ilmenite.

450

451 P-T conditions and a P-T path were established for metamorphism of the schist mylonite (sample
 452 CS18-32) using phase equilibrium modeling with the following solution models: Gt(HP),
 453 Chl(HP), Mica(CHA1), Bio(TCC), feldspar, St(HP), Ctd(HP), IlGkPy, and Ep(HP) (Fuhrman &
 454 Lindsley, 1988; Holland & Powell, 1998; Tajčmanová et al., 2009; Auzanneau et al., 2010). The
 455 modeled sample contains no graphite, but apatite is present and therefore the corresponding
 456 amount of CaO bonded to P₂O₅ observed in the whole-rock analysis was subtracted from the
 457 bulk composition (Table S5). Since garnet cores (and mantles) and rims represent different
 458 metamorphic stages with respect to S₃, they were modeled in two separate P-T sections (Fig. 8).
 459 Note that these calculations have an uncertainty of ±50 °C (Powell & Holland, 2008; Palin et al.,
 460 2016). Garnet core and mantle P-T conditions were modeled in the system MnO-Na₂O-CaO-
 461 K₂O-FeO-MgO-Al₂O-SiO₂-TiO₂-H₂O with H₂O as a saturated phase (Fig. 8a). Measured garnet
 462 core compositions match modeled garnet compositions at the garnet-in line between 525–540 °C
 463 and 340–370 MPa within the stability field Grt-Bt-Ms-Chl-Pl-Ilm-Qz, which is consistent with
 464 the presence of ilmenite inclusions in garnet cores. The increase in X_{Mg} and almandine content
 465 and decrease in spessartine and grossular content from garnet cores through mantles indicates
 466 garnet growth during an increase in temperature to conditions of 550–565 °C and 340–370 MPa.
 467 Measured garnet mantle compositions match modeled garnet isopleths in and around phase fields
 468 that include both andalusite and staurolite, suggesting that these two minerals grew concurrent
 469 with garnet mantle growth primarily related to heating.

470

471 To account for fractionation, garnet rims were modeled separately using a bulk composition from
 472 which garnet cores and mantles were removed (Fig. 8b). Based on thin section observations and
 473 volume percentage predicted by the P-T section for garnet cores and mantles, 0.45 vol% garnet
 474 with a composition averaged from garnet cores and mantles (Alm₆₁Sps₂₂Py₉Grs₅) was subtracted
 475 from the whole rock composition. Minor magnetite present in the matrix indicates the presence
 476 of ferric iron, and it is also therefore appropriate to consider the redox budget in the calculation.
 477 O₂ content was estimated from a T-X_{O₂} section at 400 MPa calculated for the new bulk
 478 composition (Fig. S4). The stability of magnetite and the garnet rim compositions suggest that

479 between 0.04 and 0.10 wt% O₂ may have been present in the system during shearing. We
480 therefore added 0.07 wt% O₂ to the bulk composition to estimate P-T conditions of garnet rim
481 growth and shearing.

482
483 The decrease in pyrope content and increase in grossular content in the garnet growth rims
484 relative to the mantles indicates an increase in pressure during development of S₃, which
485 destabilized andalusite and staurolite. The garnet rim compositions plot at the now higher-
486 temperature garnet-in line (from fractionation), recording P-T conditions of 550–570 °C and
487 450–490 MPa with the following phases stable: Grt-Bt-Ms-Chl-Pl-Mag-Qz, which is consistent
488 with the S₃ mineral assemblage (Fig. 8b). Matrix biotite compositions ($X_{Mg} = 0.46–0.49$) match
489 corresponding isopleths that are mostly consistent with this garnet rim estimate, plotting at only
490 slightly higher temperatures (570–590 °C). This estimate indicates the peak pressure recorded by
491 garnet growth related to shearing deformation, although the presence of minor rutile in the
492 sample suggests conditions may have reached higher pressures (above 700–900 MPa). However,
493 the lack of evidence of equilibration in other minerals makes these conditions impossible to
494 estimate, but the P-T modeling shows a clear pattern of an initial phase of heating, followed by a
495 near-isothermal pressure increase.

496
497 Peak temperature estimates were also calculated from the Ti content of biotite following the
498 method of Henry et al. (2005). Biotite grains selected for geothermometry were inclusion-free,
499 showed no retrogression textures, and were not in contact with garnet. The Ti contents suggest
500 peak metamorphic temperatures were primarily between 550–600 °C with an error of ± 24 °C
501 (Fig. 9; Table S6). This temperature estimate is consistent across the four samples from the LRS
502 mylonite and matches the temperature range predicted by the phase equilibrium modeling.

503
504 The metabasalt mylonites contain a syn-kinematic mineral assemblage of amphibole +
505 plagioclase + epidote + titanite \pm chlorite \pm quartz. Large amphibole porphyroblasts have
506 chemically distinct cores and tails (Fig. 6b) and sometimes contain inclusions of titanite and
507 plagioclase (Fig. 6c). Fine-grained amphibole, plagioclase, epidote, titanite, and ilmenite
508 surround the amphibole porphyroblasts. Titanite and ilmenite occur as discontinuous seams often
509 wrapping around amphibole grains with titanite sometimes enveloping large ilmenite grains.

510 Quartz and chlorite occur as minor phases, with quartz present as fine grains within the matrix
 511 and rare chlorite present along amphibole tails. Fine-grained layers of epidote and amphibole
 512 with interspersed ribbons of plagioclase may represent relict epidote veins (Fig. 6d).

513
 514 P-T conditions during metamorphism of the metabasalt mylonite were constrained with
 515 amphibole and plagioclase compositions (Fig. 10; Table S7 and S8). Spot analyses and maps
 516 document increasing Fe, Al, Ti, and Na content and decreasing Mg and Si content from
 517 amphibole cores to rims/tails (Fig. 10a,c). The Si, Al, and Na distribution in amphibole structural
 518 sites depends on the pressure and temperature during growth (Ernst & Liu, 1998; Spear, 1981,
 519 1995). Amphibole transitions from actinolite cores to hornblende/tschermakite rims via the
 520 pressure-sensitive Al-Tschermak substitution (${}^T\text{Si} + {}^{M1-M3}\text{Mg} = {}^T\text{Al} + {}^{M1-M3}\text{Al}$). The positive
 521 correlation between A site occupancy and tetrahedrally-coordinated Al (Al^{IV}) records the
 522 temperature-sensitive edenite exchange (${}^T\text{Si} + {}^{\text{A}}[\] = {}^T\text{Al} + {}^{\text{A}}(\text{Na} + \text{K})$). Growth of magnesio-
 523 hornblende amphibole rims suggests peak metamorphic temperatures were >420 °C, providing a
 524 minimum constraint (Maruyama et al., 1983). Additionally, TiO_2 in amphibole increases from
 525 0.05–0.15 in the cores to 0.20–0.50 in the rims. The increasing TiO_2 content is consistent with
 526 increasing temperature (Ernst & Liu, 1998). These trends record prograde amphibole growth
 527 during deformation. Metamorphic plagioclase compositions are oligoclase to andesine (An_{26-45} ;
 528 Fig. 10b), which are typical of amphibolite facies metamorphism and the calcification of
 529 plagioclase, caused by increasing temperature, is consistent with the actinolite-to-hornblende
 530 transition (Maruyama et al., 1982; Maruyama et al., 1983; Spear, 1995).

531 **6 Discussion**

532 *6.1 The Leech River Shear Zone: a paleo-subduction thrust*

533 Our field and microstructural observations are the first to document reverse-sinistral
 534 displacement across the LRSZ and define the LRSZ as a high strain zone distinct from the
 535 surrounding rocks. The kinematic interpretation is based on the steeply plunging lineation, north-
 536 side-up reverse-sense kinematic indicators in sub-vertical exposures, and sinistral-sense
 537 indicators in sub-horizontal exposures. We interpret the thinner, more repetitive compositional
 538 layering, composite foliations, and finer grain size in the schist mylonite to be the result of higher
 539 shear strain accumulated during further isoclinal folding, layer thinning, and transposition

540 relative to the folding and disruption of bedding observed in the schist north of the LRSZ. The S_2
541 foliation in the Leech River Schist north of the mylonite zone is parallel to the mylonitic foliation
542 (S_3) in both the schist and metabasalt mylonites, and the vergence direction throughout the schist
543 and within the mylonite zone are similar, indicating that deformation of the entire package
544 involved one predominant shortening direction with higher strain localized in the LRSZ. These
545 interpretations are broadly consistent with previous observations (Fairchild & Cowan, 1982;
546 Groome et al., 2003), though our results establish the importance of the reverse-sense motion
547 across the LRSZ.

548

549 Metamorphic conditions in the schist and metabasalt mylonites in the LRSZ are consistent with
550 deformation at amphibolite facies. In the schist mylonites, metamorphism involved an initial
551 phase of heating at low pressure to amphibolite facies conditions, resulting in the pre-kinematic
552 growth of biotite, staurolite, andalusite, and garnet (cores and mantles), followed by a sharp
553 increase in pressure, resulting in the destabilization of staurolite and andalusite and syn-
554 kinematic growth of muscovite, chlorite, biotite, and garnet (rims). This progression outlines a
555 qualitative anticlockwise P-T path. Temperature and pressure estimates of 550–570 °C and 450–
556 490 MPa from garnet rim compositions (Fig. 8) are further supported by peak temperature
557 estimates of 550–575 °C from Ti-in-biotite geothermometry (Fig. 9). In the metabasalt
558 mylonites, the transition from actinolite cores to hornblende rims in porphyroclasts indicates the
559 transition from greenschist to amphibolite facies (Fig. 10). Similar P-T conditions during syn-
560 kinematic mineral growth in both the schist and metabasalt mylonites demonstrate that strain
561 caused by reverse-sense motion was distributed across both units at peak P-T.

562

563 The metamorphic mineralogy of the schist and metabasalt mylonites is consistent with previous
564 observations of the Leech River Schist and Metchosin Basalt from outside the LRSZ (Fairchild
565 & Cowan, 1982; Rusmore & Cowan, 1985; Groome et al., 2003; Timpa et al., 2005). However,
566 previous P-T estimates for the Leech River Schist were restricted to high-temperature, low-
567 pressure metamorphism based on the presence of andalusite (Fairchild & Cowan, 1982; Groome
568 et al., 2003). Our observations show that andalusite in the schist mylonite is rare, small (<1 cm),
569 and exhibits disequilibrium textures, with chlorite and muscovite replacing andalusite and
570 forming syn-kinematic tails (e.g., Fig. 5e). We therefore interpret andalusite growth to pre-date

571 syn-kinematic metamorphism in the LRSZ, which is associated with a pressure increase of at
572 least 100–200 MPa, or higher, based on the presence of rutile. This increase in burial depth after
573 the high T, low P metamorphism suggests upper plate thickening associated with the
574 underthrusting of the MIC occurred before and during the final docking of the MIC basalts in
575 their current position relative to the structurally overlying LRC.

576

577 P-T estimates for the schist mylonites correspond to a geothermal gradient of ~30 °C/km when
578 the LRSZ was active, which is higher than the hottest modern subduction zones (Penniston-
579 Dorland et al., 2015; Syracuse et al., 2010). However, geothermal gradients as high as 50 °C/km
580 during ridge subduction have been reported in other subduction complexes (e.g., Sisson et al.,
581 1989; Pavlis & Sisson, 1995; Sakaguchi, 1996; Brown, 1998; Zumsteg et al., 2003). The elevated
582 temperatures estimated from the LRSZ are likely due to the anomalously high geothermal
583 gradients produced by subduction of the Kula/Resurrection-Farallon Ridge beneath the forearc,
584 the young age of the subducting plate, and the nearby Yellowstone hotspot (Breitsprecher et al.,
585 2003; Groome & Thorkelson, 2009).

586

587 The southward increase in metamorphic grade from greenschist to amphibolite facies in the LRS
588 does not exhibit the inverted thermal gradient typical of subduction systems (Peacock, 1987). We
589 suggest that the regional thermal structure of the LRC was established by heating from below by
590 a young, hot, plume-affected oceanic plate, rather than refrigeration by a cold slab. Throughout
591 the LRC, isoclinal, asymmetric folds with top-to-the-south vergence appear to have developed
592 either prior to and/or at the local peak conditions, representing regional shortening during burial.
593 The consistency of the attitudes of the S_2 regional foliation with the S_3 mylonitic foliation
594 suggests this shortening could have occurred within the upper plate during convergence.
595 Throughout the LRC, isoclinal, asymmetric folds with top-to-the-south vergence are consistent
596 with shortening of the upper plate during convergence. The late near-isothermal increase in
597 pressure recorded by the mylonites was likely due to tectonic burial by wedge shortening and
598 thickening during underthrusting as strain localized onto the LRSZ. This interpretation implies
599 the noncoaxial deformation in the LRSZ during the syn-kinematic growth of garnet rims only
600 records the latest phase in the subduction history of the MIC as it progressed from the trench to
601 peak P-T conditions.

602

603 Overall, the shear zone kinematics and anticlockwise P-T path with heating followed by a
604 pressure increase, combined with the juxtaposition of a fragment of oceanic crust against an
605 underplated terrigenous complex, all suggest that the LRSZ is a sinistral-oblique thrust that
606 accommodated underthrusting of the Siletz-Crescent terrane beneath the North American margin
607 in a subduction zone setting. The kinematics and syn-kinematic prograde metamorphic
608 conditions inferred in both lithologies within the LRSZ are inconsistent with alternative
609 hypotheses for the LRSZ tectonic setting (i.e., dominantly strike-slip motion (e.g., Fairchild &
610 Cowan, 1982) or development as part of a forearc rift (e.g., Babcock et al., 1992)). Although the
611 thermal history of the LRSZ is atypical of subduction assemblages, we conclude that the LRSZ
612 represents a hot paleo-subduction interface.

613 *6.2 Tectonic history of the Leech River Complex and Leech River Shear Zone*

614 The LRSZ forms the tectonic contact between the LRC and MIC of the Siletz-Crescent terrane
615 and therefore its deformation history can be used to inform the tectonic history of the
616 surrounding units. Our results provide new constraints on the origin of the LRC. Detrital zircon
617 U-Pb ages indicate an early Paleocene MDA for the Leech River Schist and Jordan River Unit of
618 the LRC, which is significantly younger than previously reported Late Jurassic to Cretaceous
619 deposition estimates based on whole-rock Rb-Sr isotopic data (Fairchild & Cowan, 1982) and
620 youngest zircon U-Pb ages (Groome et al., 2003). These new ages for the LRC place an upper
621 bound on when the LRSZ was active, and they are broadly consistent with underthrusting of the
622 MIC in the Eocene (Eddy et al., 2017).

623

624 Detrital zircon age distributions from the LRC provide further constraints on its depositional
625 context and further tests whether the LRC is an allochthonous terrane. The LRC has a similar age
626 distribution to two groups of sedimentary rocks: the youngest (Maastrichtian- to early Paleocene-
627 age) formations in the Upper Nanaimo Group on Vancouver Island (Coutts et al., 2020; Englert
628 et al., 2018; Matthews et al., 2017) and the Yakutat Group in Alaska, which has previously been
629 correlated with the Pacific Rim terrane (Garver & Davidson, 2015). The Upper Nanaimo Group
630 was deposited in a marine subduction forearc basin (Coutts et al., 2020). The Yakutat Group,
631 part of the Chugach-Prince William terrane, was deposited as trench-fill turbidites, then

632 incorporated into an accretionary complex (Garver & Davidson, 2015). The LRC shares similar
633 MDA, peaks in Proterozoic ages at 1850–1560 Ma and 1450–1300 Ma, and absence of grains
634 with 1000–1300 Ma ages with these units (Fig. 3b). For both the Upper Nanaimo Group and
635 Yakutat Group, previous work interpreted detrital zircon grains with Mesozoic and early
636 Paleocene ages (200–60 Ma) to be derived from the Coast Mountains Batholith, while
637 Proterozoic (1850–1560 and 1450–1300 Ma) zircons were interpreted to be sourced from the
638 Yavapai and Mazatzal terranes of southwestern Laurentia (Cou tts et al., 2020; Dumitru et al.,
639 2016; Garver & Davidson, 2015; Housen & Beck, 1999; Matthews et al., 2017). It is important
640 to note that the source of these Proterozoic-age zircons and the paleolatitude of the Nanaimo
641 Group is an ongoing debate. However, we suggest these interpretations of detrital zircon source
642 regions are also applicable to the LRC.

643
644 The LRC was previously interpreted as allochthonous to Vancouver Island (Fairchild & Cowan,
645 1982), but these new detrital zircon ages support an alternative interpretation. We suggest the
646 similar detrital zircon age distributions (and therefore similar sources) of the LRC and Upper
647 Nanaimo Group as demonstrate that these units were derived from similar sedimentary sources,
648 and therefore likely deposited near each other in the latest Cretaceous to early Paleocene. This
649 model also implies that the LRC was deposited in proximity to the Wrangellia terrane, which
650 constitutes the majority of Vancouver Island, as the Nanaimo Group uncomfortably overlies the
651 Wrangellia terrane (Mustard, 1994). Our data do not directly test whether there has been any
652 relative motion between the LRC and Wrangellia; however, the simplest explanation for the
653 similarity between the LRC and Nanaimo Group ages is that the LRC represents a marine
654 sequence that shared the same source region at the same time as the Nanaimo Group basin. This
655 tectonic context, the mixed lithologies of the LRC (psammitic, pelitic, and mafic volcanics), and
656 the similar depositional age of the Upper Nanaimo suggest the LRC represents an assemblage of
657 metamorphosed marine basin rocks, likely deposited in a near-margin trench environment.
658 Within the LRC, the structural record of block-in-matrix textures, transposition of bedding, and
659 layer-perpendicular veins, which are typical of underthrust subduction complexes (e.g.,
660 Connelly, 1978; Fisher & Byrne, 1987; Pavlis & Sisson, 1995; Meneghini et al., 2009; Ujiie,
661 2002). Furthermore, the LRS depositional age is broadly correlative with the Chugach
662 accretionary complex, and possibly parts of the Franciscan complex, which together record

663 subduction off the west coast of North America in the latest Cretaceous and Paleocene (Cowan,
664 1982, 2003; Garver & Davidson, 2015). We therefore conclude that the LRC is not as an
665 allochthonous terrane, but represents an accretionary complex developed from trench-fill
666 sediments consistent with the North American margin.

667
668 We summarize our results with available timing constraints on the tectonic history of the LRC,
669 Siletz-Crescent, and LRSZ from the literature (Fig. 11). At ~65–60 Ma (Fig. 11a), the Leech
670 River Schist (MDA ~66–61 Ma) and Upper Nanaimo Group (MDA ~80–64 Ma) were deposited
671 in near-margin trench and forearc basins, respectively, with the Nanaimo Group unconformably
672 overlying the Wrangellia terrane (this study; Coutts et al., 2020; Englert et al., 2018; Matthews et
673 al., 2017). Any northward coast-wise transport of all three units occurred during oblique
674 subduction (Coutts et al., 2020; Matthews et al., 2017). At ~52 Ma (Fig. 11b), the Metchosin
675 Basalt was erupted as part of an oceanic plateau (U-Pb zircon age of 52 ± 2 Ma; Massey, 1986),
676 while the LRC was underthrust and deformed as an accretionary complex during subduction of
677 the Kula/Resurrection and Farallon plates, and the Nanaimo Group was shallowly buried
678 (Stewart & Page, 1974). The Kula/Resurrection-Farallon ridge (and slab window) was subducted
679 ahead of the Metchosin Basalt. By ~51–48 Ma (Fig. 11c), during the accretion of the Siletz-
680 Crescent terrane to the North American margin (Eddy et al., 2017), the Metchosin Basalt was
681 subducted beneath the Leech River Schist along the LRSZ, and the Cowichan fold-and-thrust
682 belt developed in the Nanaimo Group (England & Calon, 1991). Shortening and thickening of
683 the upper plate buried the active LRSZ, causing a near-isothermal pressure increase during shear.
684 Shortly thereafter, the Metchosin Basalt, and the LRSZ itself, were underplated and accreted to
685 the overriding continent as the décollement stepped further west. Emplacement of the Walker
686 Creek intrusions pin the location of the schist to its current latitude from ~51 Ma to the present
687 (Breitsprecher et al., 2003; Groome et al., 2003). Additionally, some of these intrusions exhibit
688 deformation while others are not deformed (Groome et al., 2003), indicating syn- to post-
689 kinematic emplacement and marking the cessation of deformation in the LRSZ and underplating
690 of the Metchosin Basalt. Following underplating, the LRC was exhumed through the mica
691 cooling temperatures ($^{40}\text{Ar}/^{39}\text{Ar}$ ages of 45.2 ± 0.2 Ma and 42.5 ± 0.2 Ma in muscovite and biotite,
692 respectively; Groome et al., 2003). Exhumation may have been accommodated by a structurally
693 lower fault during subsequent subduction (e.g. at the base of the MIC), though this is currently

694 untested. Unconformable deposition of the coastal marine Carmanah Group across the LRSZ in
695 the Oligocene constrains the exposure of the units at the surface (Fig. 11d; Harrichhausen, 2021;
696 Muller, 1977a). The compatibility of this re-interpretation with previous work on the tectonic
697 history and timing of accretion of the Siletz-Crescent terrane (Eddy et al., 2016; Groome et al.,
698 2003; McCrory & Wilson, 2013; Wells et al., 2014), reinforces the interpretation that the LRSZ
699 was a hot subduction plate boundary interface in the Eocene.

700 **7 Conclusions**

701 This study evaluates the LRSZ as a possible paleo-subduction interface. Structural, kinematic,
702 and petrologic evidence from the LRSZ indicates hot rocks underwent reverse-sinistral sense
703 deformation during a near-isothermal pressure increase at amphibolite facies conditions related
704 to underthrusting during subduction. The elevated geothermal gradient implied by the P-T
705 conditions likely resulted from subduction of the Kula/Resurrection-Farallon Ridge, subsequent
706 formation of a slab window, and the nearby Yellowstone Hotspot. These observations are
707 consistent with tectonic models of the hotspot location and plate motions during the Eocene (~50
708 Ma). Detrital zircon age distributions suggest the Leech River Schist is a Paleocene-age
709 accretionary complex that was deposited in proximity to the Upper Nanaimo Group and
710 Wrangellia terrane, and therefore the LRC is not allochthonous to Vancouver Island. Overall, we
711 establish that the LRSZ represents a paleo-subduction interface from an anomalously hot Eocene
712 subduction zone.

713 **Acknowledgements**

714 We thank TimberWest and Hydro BC for assistance in accessing the field area. C.S.
715 acknowledges support from the Fonds de recherche du Québec – Nature et technologies
716 (FRQNT). J.K. acknowledges support from the Natural Sciences and Engineering Research
717 Council of Canada (NSERC), Discovery Grant RGPIN-2022-04193. D.S. acknowledges support
718 from an NSERC Undergraduate Student Research Award (USRA). A.L. acknowledges support
719 from the University of Washington and thanks Tamas Ugrai and Samuel Shekut for assistance in
720 the lab. C.R. acknowledges support from NSF EAR IRFP Grant #1349586 and NSF EAR
721 Tectonics Grant #1756834. Thanks to Sarah Roeske and an anonymous reviewer for constructive
722 reviews that greatly improved the manuscript.

723 **Open Research**

724 The whole rock compositional data, mineral composition data, detrital zircon U-Pb analyses, and
 725 structural data are available in the supplementary information. The geochemical data (whole
 726 rock, mineral, and detrital zircon U-Pb) are also available through the EarthChem
 727 (<https://doi.org/10.26022/IEDA/112312>). *PerpleX* version 6.9.9 (Connolly, 2005) was used for
 728 phase equilibrium modeling and is developed openly at <https://www.perplex.ethz.ch/>.

729 **References**

- 730 Auzanneau, E., Schmidt, M. W., Vielzeuf, D., & Connolly, J. A. D. (2010). Titanium in
 731 phengite: a geobarometer for high temperature eclogites. *Contributions to Mineralogy
 732 and Petrology*, 159(1), 1. <https://doi.org/10.1007/s00410-009-0412-7>
- 733 Babcock, R. S., Burmester, R. F., Engebretson, D. C., Warnock, A., & Clark, K. P. (1992). A
 734 rifted margin origin for the crescent basalts and related rocks in the northern Coast Range
 735 Volcanic Province, Washington and British Columbia. *Journal of Geophysical Research:
 736 Solid Earth*, 97(B5), 6799-6821. <https://doi.org/10.1029/91JB02926>
- 737 Behr, W. M., Holt, A. F., Becker, T. W., & Faccenna, C. (2022). The effects of plate interface
 738 rheology on subduction kinematics and dynamics. *Geophysical Journal International*,
 739 230(2), 796-812. <https://doi.org/10.1093/gji/ggac075>
- 740 Breitsprecher, K., Thorkelson, D. J., Groome, W. G., & Dostal, J. (2003). Geochemical
 741 confirmation of the Kula-Farallon slab window beneath the Pacific Northwest in Eocene
 742 time. *Geology*, 31(4), 351-354. [https://doi.org/10.1130/0091-
 743 7613\(2003\)031<0351:GCOTKF>2.0.CO;2](https://doi.org/10.1130/0091-7613(2003)031<0351:GCOTKF>2.0.CO;2)
- 744 Brown, M. (1998). Ridge–trench interactions and high-T–low-P metamorphism, with particular
 745 reference to the Cretaceous evolution of the Japanese Islands. *Geological Society,
 746 London, Special Publications*, 138, 137-169.
 747 <https://doi.org/10.1144/GSL.SP.1996.138.01.09>
- 748 Cecil, M. R., Rusmore, M. E., Gehrels, G., Woodsworth, G., Stowell, H. H., Yokelson, I. N., et
 749 al. (2018). Along-strike variation in the magmatic tempo of the Coast Mountains
 750 Batholith, British Columbia, and implications for processes controlling episodicity in
 751 arcs. *Geochemistry, Geophysics, Geosystems*, 19(11), 4274-4289.
 752 <https://doi.org/10.1029/2018GC007874>

- 753 Chelle-Michou, C., McCarthy, A., Moyen, J.-F., Cawood, P. A., & Capitanio, F. A. (2022).
 754 Make subductions diverse again. *Earth-Science Reviews*, 226, 103966.
 755 <https://doi.org/10.1016/j.earscirev.2022.103966>
- 756 Clowes, R. M., Brandon, M. T., Green, A. G., Yorath, C. J., Brown, A. S., Kanasewich, E. R., &
 757 Spencer, C. (1987). LITHOPROBE--southern Vancouver Island: Cenozoic subduction
 758 complex imaged by deep seismic reflections. *Canadian Journal of Earth Sciences*, 24(1),
 759 31-51. <https://doi.org/10.1139/e87-004>
- 760 Connelly, W. (1978). Uyak Complex, Kodiak Islands, Alaska: A Cretaceous subduction
 761 complex. *Geological Society of America Bulletin*, 89(5), 755-769.
 762 [https://doi.org/10.1130/0016-7606\(1978\)89<755:UCKIAA>2.0.CO;2](https://doi.org/10.1130/0016-7606(1978)89<755:UCKIAA>2.0.CO;2)
- 763 Connolly, J. A. D. (2005). Computation of phase equilibria by linear programming: a tool for
 764 geodynamic modeling and its application to subduction zone decarbonation. *Earth and*
 765 *Planetary Science Letters*, 236, 524-541. <https://doi.org/10.1016/j.epsl.2005.04.033>
- 766 Coutts, D., Matthews, W. A., Englert, R. G., Brooks, M. D., Boivin, M.-P., & Hubbard, S.
 767 (2020). Along-strike variations in sediment provenance within the Nanaimo basin reveal
 768 mechanisms of forearc basin sediment influx events. *Lithosphere*, 12(1), 180-197.
 769 <https://doi.org/10.1130/L1138.1>
- 770 Cowan, D. S. (1982). Geological evidence for post-40 m.y. B.P. large-scale northwestward
 771 displacement of part of southeastern Alaska. *Geology*, 10, 309-313.
 772 [https://doi.org/10.1130/0091-7613\(1982\)10<309:GEFPMB>2.0.CO;2](https://doi.org/10.1130/0091-7613(1982)10<309:GEFPMB>2.0.CO;2)
- 773 Cowan, D. S. (2003). Revisiting the Baranof-Leech River hypothesis for early Tertiary coastwise
 774 transport of the Chugach-Prince William terrane. *Earth and Planetary Science Letters*,
 775 213(3-4), 463-475. [https://doi.org/10.1016/S0012-821X\(03\)00300-5](https://doi.org/10.1016/S0012-821X(03)00300-5)
- 776 Cowan, D. S., Brandon, M. T., & Garver, J. I. (1997). Geologic tests of hypotheses for large
 777 coastwise displacements—A critique illustrated by the Baja British Columbia
 778 controversy. *American Journal of Science*, 297(2), 117-173.
 779 <https://doi.org/10.2475/ajs.297.2.117>
- 780 Cui, Y., Miller, D., Schiarizza, P., & Diakow, L. J. (2017). *British Columbia digital geology*.
 781 British Columbia Ministry of Energy, Mines and Petroleum Resources, British Columbia
 782 Geological Survey Open File 2017-8, Data version 2019-12-19.

- 783 DeLong, S. E., Schwarz, W. M., & Anderson, R. N. (1979). Thermal effects of ridge subduction.
784 *Earth and Planetary Science Letters*, 44, 239-246. <https://doi.org/10.1016/0012->
785 821X(79)90172-9
- 786 Dumitru, T. A., Elder, W. P., Hourigan, J. K., Chapman, A. D., Graham, S. A., & Wakabayashi,
787 J. (2016). Four Cordilleran paleorivers that connected Sevier thrust zones in Idaho to
788 depocenters in California, Washington, Wyoming, and, indirectly, Alaska. *Geology*,
789 44(1), 75-78. <https://doi.org/10.1130/G37286.1>
- 790 Duncan, R. A. (1982). A captured island chain in the Coast Range of Oregon and Washington.
791 *Journal of Geophysical Research: Solid Earth*, 87(B13), 10827-10837.
792 <https://doi.org/10.1029/JB087iB13p10827>
- 793 Eddy, M. P., Bowring, S. A., Umhoefer, P. J., Miller, R. B., McLean, N. M., & Donaghy, E. E.
794 (2016). High-resolution temporal and stratigraphic record of Siletzia's accretion and triple
795 junction migration from nonmarine sedimentary basins in central and western
796 Washington. *Geological Society of America Bulletin*, 128(3-4), 425-441.
797 <https://doi.org/10.1130/B31335.1>
- 798 Eddy, M. P., Clark, K. P., & Polenz, M. (2017). Age and volcanic stratigraphy of the Eocene
799 Siletzia oceanic plateau in Washington and on Vancouver Island. *Lithosphere*, 9(4), 652-
800 664. <https://doi.org/10.1130/L650.1>
- 801 England, T. D. J., & Calon, T. J. (1991). The Cowichan fold and thrust system, Vancouver
802 Island, southwestern British Columbia. *Geological Society of America Bulletin*, 103, 336-
803 362. [https://doi.org/10.1130/0016-7606\(1991\)103<0336:TCFATS>2.3.CO;2](https://doi.org/10.1130/0016-7606(1991)103<0336:TCFATS>2.3.CO;2)
- 804 Englert, R. G., Hubbard, S., Coutts, D., & Matthews, W. A. (2018). Tectonically controlled
805 initiation of contemporaneous deep- water channel systems along a Late Cretaceous
806 continental margin, western British Columbia, Canada. *Sedimentology*, 65, 2404-2438.
807 <https://doi.org/10.1111/sed.12472>
- 808 Ernst, W. G., & Liu, J. (1998). Experimental phase-equilibrium study of Al- and Ti-contents of
809 calcic amphibole in MORB—A semiquantitative thermobarometer. *American*
810 *Mineralogist*, 83, 952-969. <https://doi.org/10.2138/am-1998-9-1004>
- 811 Evans, T. P. (2004). A method for calculating effective bulk composition modification due to
812 crystal fractionation in garnet-bearing schist: implications for isopleth thermobarometry.

- 813 *Journal of Metamorphic Geology*, 22(6), 547-557. <https://doi.org/10.1111/j.1525->
814 1314.2004.00532.x
- 815 Fairchild, L. H., & Cowan, D. S. (1982). Structure, petrology, and tectonic history of the Leech
816 River complex northwest of Victoria, Vancouver Island. *Canadian Journal of Earth*
817 *Sciences*, 19(9), 1817-1835. <https://doi.org/10.1139/e82-161>
- 818 Fisher, D., & Byrne, T. (1987). Structural evolution of underthrust sediments, Kodiak Islands,
819 Alaska. *Tectonics*, 6(6), 775-793. <https://doi.org/10.1029/TC006i006p00775>
- 820 Friedman, R. M., & Armstrong, R. L. (1995). Jurassic and Cretaceous geochronology of the
821 southern Coast Belt, British Columbia, 49° to 51°N. *Special Papers-Geological Society*
822 *of America*, 299, 95-139. <https://doi.org/10.1130/SPE299-p95>
- 823 Fuhrman, M. L., & Lindsley, D. H. (1988). Ternary-feldspar modeling and thermometry.
824 *American Mineralogist*, 73(3-4), 201-215.
- 825 Garver, J. I., & Davidson, C. M. (2015). Southwestern Laurentian zircons in Upper Cretaceous
826 flysch of the Chugach-Prince William terrane in Alaska. *American Journal of Science*,
827 315(6), 537-556. <https://doi.org/10.2475/06.2015.02>
- 828 Gehrels, G., Rusmore, M. E., Woodsworth, G., Crawford, M., Andronicos, C., Hollister, L., et al.
829 (2009). U-Th-Pb geochronology of the Coast Mountains batholith in north-coastal British
830 Columbia: Constraints on age and tectonic evolution. *Geological Society of America*
831 *Bulletin*, 121(9-10), 1341-1361. <https://doi.org/10.1130/B26404.1>
- 832 Groome, W. G. (2000). *Magmatism and Metamorphism in the Leech River Complex, Southern*
833 *Vancouver Island, British Columbia, Canada: Implications for Eocene Tectonics of the*
834 *Pacific Northwest* (Master's thesis). Vancouver, BC: Simon Fraser University.
- 835 Groome, W. G., & Thorkelson, D. J. (2009). The three-dimensional thermo-mechanical signature
836 of ridge subduction and slab window migration. *Tectonophysics*, 464, 70-83.
837 <https://doi.org/10.1016/j.tecto.2008.07.003>
- 838 Groome, W. G., Thorkelson, D. J., Friedman, R. M., Mortensen, J. K., Massey, N. W. D.,
839 Marshall, D. D., & Layer, P. W. (2003). Magmatic and tectonic history of the Leech
840 River Complex, Vancouver Island, British Columbia: Evidence for ridge-trench
841 intersection and accretion of the Crescent Terrane. *Special Papers-Geological Society of*
842 *America*, 371, 327-353. <https://doi.org/10.1130/0-8137-2371-X.327>

- 843 Harrichhausen, N. (2021). *Fault accommodation of permanent strain in the northern Cascadia*
 844 *forearc* (Doctoral thesis). (<https://escholarship.org/uc/item/5h05p9fv>). Santa Barbara,
 845 CA: University of California, Santa Barbara.
- 846 Harrichhausen, N., Morell, K. D., Regalla, C., Bennett, S. E., Leonard, L. J., Lynch, E. M., &
 847 Nissen, E. (2021). Paleoseismic trenching reveals Late Quaternary kinematics of the
 848 Leech River Fault: Implications for forearc strain accumulation in northern Cascadia
 849 *Bulletin of the Seismological Society of America*, *111*(2), 1110-1138.
 850 <https://doi.org/10.1785/0120200204>
- 851 Hawthorne, F. C., Oberti, R., Harlow, G. E., Maresch, W. V., Martin, R. F., Schumacher, J. C.,
 852 & Welch, M. D. (2012). Nomenclature of the amphibole supergroup. *American*
 853 *Mineralogist*, *97*, 2031-2048. <http://doi.org/10.2138/am.2012.4276>
- 854 Henry, D. J., Guidotti, C. V., & Thomson, J. A. (2005). The Ti-saturation surface for low-to-
 855 medium pressure metapelitic biotites: Implications for geothermometry and Ti-
 856 substitution mechanisms. *American Mineralogist*, *90*(2-3), 316-328.
 857 <https://doi.org/10.2138/am.2005.1498>
- 858 Holland, T. J. B., & Powell, R. (1998). An internally consistent thermodynamic data set for
 859 phases of petrological interest. *Journal of Metamorphic Geology*, *16*(3), 309-343.
 860 <https://doi.org/10.1111/j.1525-1314.1998.00140.x>
- 861 Holt, A. F., & Condit, C. B. (2021). Slab temperature evolution over the lifetime of a subduction
 862 zone. *Geochemistry, Geophysics, Geosystems*, *22*(6), e2020GC009476.
 863 <https://doi.org/10.1029/2020GC009476>
- 864 Horstwood, M. S. A., Košler, J., Gehrels, G., Jackson, S. E., McLean, N. M., Paton, C., et al.
 865 (2016). Community- Derived Standards for LA- ICP- MS U- (Th-)Pb Geochronology
 866 – Uncertainty Propagation, Age Interpretation and Data Reporting. *Geostandards and*
 867 *Geoanalytical Research*, *40*(3), 311-332. <https://doi.org/10.1111/j.1751->
 868 [908X.2016.00379.x](https://doi.org/10.1111/j.1751-908X.2016.00379.x)
- 869 Housen, B., & Beck, M. E. (1999). Testing terrane transport: An inclusive approach to the Baja
 870 B.C. controversy. *Geology*, *27*(12), 1143-1146. <https://doi.org/10.1130/0091->
 871 [7613\(1999\)027<1143:TTTAIA>2.3.CO;2](https://doi.org/10.1130/0091-7613(1999)027<1143:TTTAIA>2.3.CO;2)

- 872 Hyndman, R. D., Yorath, C. J., Clowes, R. M., & Davis, E. E. (1990). The northern Cascadia
873 subduction zone at Vancouver Island: seismic structure and tectonic history. *Canadian*
874 *Journal of Earth Sciences*, 27(3), 313-329. <https://doi.org/10.1139/e90-030>
- 875 Irving, E. (1979). Paleopoles and paleolatitudes of North America and speculations about
876 displaced terrains. *Canadian Journal of Earth Sciences*, 16(3), 669-694.
877 <https://doi.org/10.1139/e79-065>
- 878 Leake, B. E., Woolley, A. R., Arps, C. E. S., Birch, W. D., Gilbert, M. C., Grice, J. D., et al.
879 (1997). Nomenclature of amphiboles: Report of the subcommittee on amphiboles of the
880 International Mineralogical Association, Commission on new minerals and mineral
881 names. *Mineralogical Magazine*, 61(405), 295-310.
882 <https://doi.org/10.1180/minmag.1997.061.405.13>
- 883 Li, G., Liu, Y., Regalla, C., & Morell, K. D. (2018). Seismicity relocation and fault structure
884 near the Leech River Fault Zone, southern Vancouver Island. *Journal of Geophysical*
885 *Research: Solid Earth*, 123, 2841-2855. <https://doi.org/10.1002/2017JB015021>
- 886 Locock, A. J. (2014). An Excel spreadsheet to classify chemical analyses of amphiboles
887 following the IMA 2012 recommendations. *Computers & Geosciences*, 62, 1-11.
888 <https://doi.org/10.1016/j.cageo.2013.09.011>
- 889 Ludwig, K. R. (2003). User's manual for Isoplot 3.00, a geochronological toolkit for Microsoft
890 Excel. 4, 25-32.
- 891 Maruyama, S., Liou, J. G., & Suzuki, O. (1982). The peristerite gap in low-grade metamorphic
892 rocks. *Contributions to Mineralogy and Petrology*, 81, 268-276.
893 <https://doi.org/10.1007/BF00371681>
- 894 Maruyama, S., Suzuki, K., & Liou, J. G. (1983). Greenschist-amphibolite transition equilibria at
895 low pressures. *Journal of Petrology*, 24(4), 583-604.
896 <https://doi.org/10.1093/petrology/24.4.583>
- 897 Massey, N. W. D. (1986). Metchosin Igneous Complex, southern Vancouver Island: Ophiolite
898 stratigraphy developed in an emergent island setting. *Geology*, 14(7), 602-605.
899 [https://doi.org/10.1130/0091-7613\(1986\)14%3C602:MICSVI%3E2.0.CO;2](https://doi.org/10.1130/0091-7613(1986)14%3C602:MICSVI%3E2.0.CO;2)
- 900 Matharu, G., Bostock, M. G., Christensen, N. I., & Tromp, J. (2014). Crustal anisotropy in a
901 subduction zone forearc: Northern Cascadia. *Journal of Geophysical Research: Solid*
902 *Earth*, 119, 7058-7078. <https://doi.org/10.1002/2014JB011321>

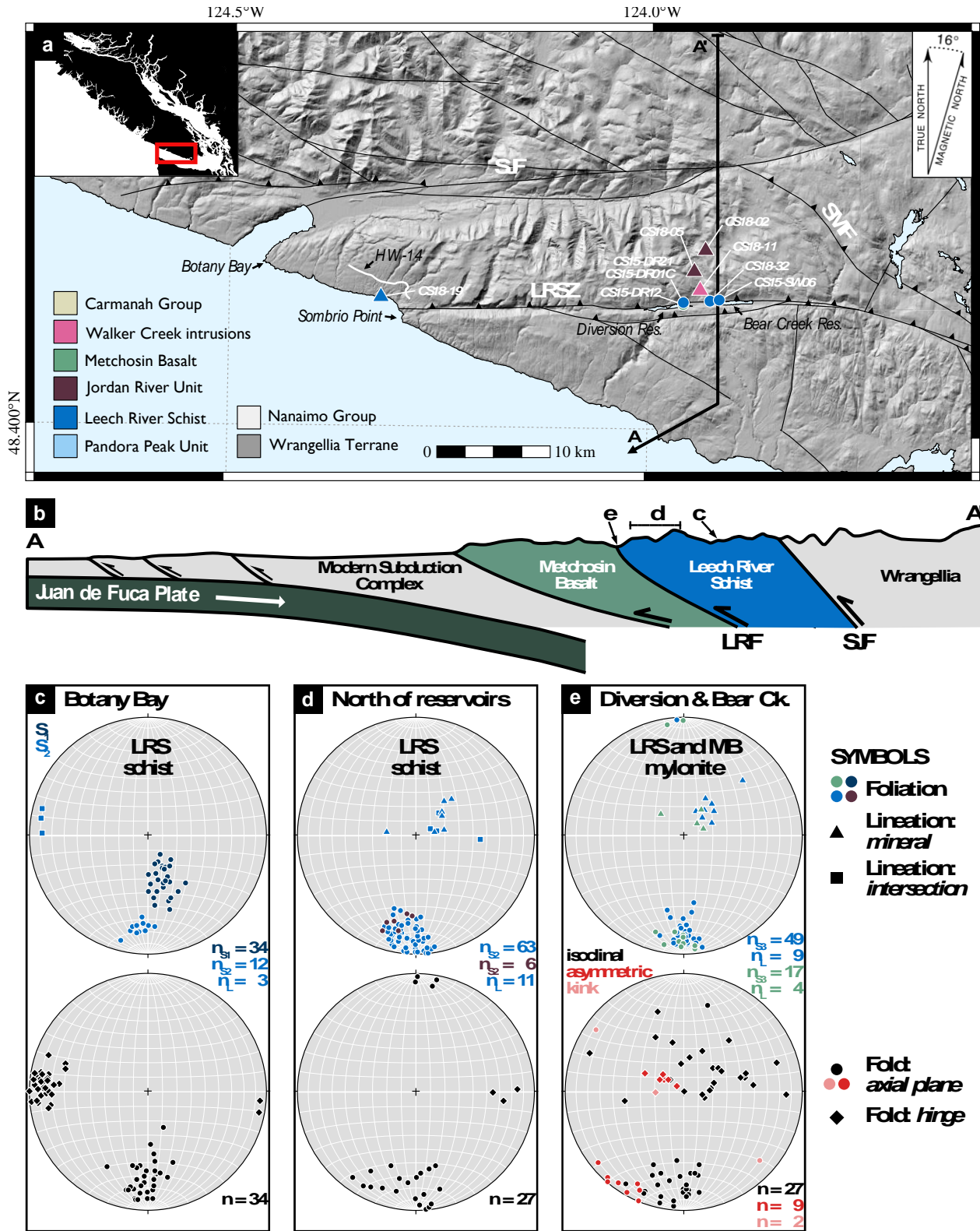
- 903 Matthews, W. A., & Guest, B. (2017). A Practical Approach for Collecting Large- n Detrital
904 Zircon U- Pb Data sets by Quadrupole LA- ICP- MS. *Geostandards and Geoanalytical*
905 *Research*, 41(2), 161-180. <https://doi.org/10.1111/ggr.12146>
- 906 Matthews, W. A., Guest, B., Coutts, D., Bain, H., & Hubbard, S. (2017). Detrital zircons from
907 the Nanaimo basin, Vancouver Island, British Columbia: An independent test of Late
908 Cretaceous to Cenozoic northward translation. *Tectonics*, 36(5), 854-876.
909 <https://doi.org/10.1002/2017TC004531>
- 910 McCrory, P. A., & Wilson, D. S. (2013). A kinematic model for the formation of the Siletz-
911 Crescent forearc terrane by capture of coherent fragments of the Farallon and
912 Resurrection plates. *Tectonics*, 32(3), 718-736. <https://doi.org/10.1002/tect.20045>
- 913 Meneghini, F., Marroni, M., Moore, J. C., Pandolfi, L., & Rowe, C. D. (2009). The processes of
914 underthrusting and underplating in the geologic record: structural diversity between the
915 Franciscan Complex (California), the Kodiak Complex (Alaska) and the Internal Ligurian
916 Units (Italy). *Geological Journal*, 44(2), 126-152. <http://doi.org/10.1002/gj.1144>
- 917 Morell, K. D., Regalla, C., Amos, C., Bennett, S. E., Leonard, L. J., Graham, A., et al. (2018).
918 Holocene surface rupture history of an active forearc fault redefines seismic hazard in
919 southwestern British Columbia, Canada. *Geophysical Research Letters*, 45, 11605-
920 11611. <https://doi.org/10.1029/2018GL078711>
- 921 Morell, K. D., Regalla, C., Leonard, L. J., Amos, C., & Levson, V. (2017). Quaternary rupture of
922 a Crustal Fault beneath Victoria, British Columbia, Canada. *GSA Today*, 27(3), 4-10.
923 <https://doi.org/10.1130/GSATG291A.1>
- 924 Muller, J. E. (1977a). Evolution of the Pacific Margin, Vancouver Island, and adjacent regions.
925 *Canadian Journal of Earth Sciences*, 14(9), 2062-2085. <http://doi.org/10.1139/e77-176>
- 926 Muller, J. E. (1977b). Geology of Vancouver Island, British Columbia. *Geological Survey of*
927 *Canada, Open File 463*. <https://doi.org/10.4095/129265>
- 928 Muller, J. E. (1980). Geology, Victoria, British Columbia. *Geological Survey of Canada, Open*
929 *File 701*. <https://doi.org/10.4095/129114>
- 930 Mustard, P. S. (1994). The Upper Cretaceous Nanaimo Group, Georgia Basin. In J. Monger
931 (Ed.), *Geology and geological hazards of the Vancouver region, southwestern British*
932 *Columbia* (pp. 320). Geological Survey of Canada Bulletin 481. Retrieved from
933 <https://doi.org/10.4095/203244>. doi:10.4095/203244

- 934 Nelson, J., & Colpron, M. (2007). Tectonics and metallogeny of the British Columbia, Yukon,
935 and Alaskan Cordillera, 1.8 Ga to the present. In W. D. Goodfellow (Ed.), *Mineral*
936 *Deposits of Canada: A Synthesis of Major Deposit-Types, District Metallogeny, the*
937 *Evolution of Geological Provinces, and Exploration Methods* (pp. 755-791). St. John's,
938 NL: Geological Association of Canada, Mineral Deposits Division, Special Publication
939 No. 5.
- 940 Palin, R. M., Weller, O. M., Waters, D. J., & Dyck, B. (2016). Quantifying geological
941 uncertainty in metamorphic phase equilibria modelling; a Monte Carlo assessment and
942 implications for tectonic interpretations. *Geoscience Frontiers*, 7, 591-607.
943 <https://doi.org/10.1016/j.gsf.2015.08.005>
- 944 Paton, C., Woodhead, J. D., Hellstrom, J. C., Hergt, J. M., Greig, A., & Maas, R. (2010).
945 Improved laser ablation U- Pb zircon geochronology through robust downhole
946 fractionation correction. *Geochemistry, Geophysics, Geosystems*, 11(3).
947 <https://doi.org/10.1029/2009GC002618>
- 948 Pavlis, T. L., & Sisson, V. B. (1995). Structural history of the Chugach metamorphic complex in
949 the Tana River region, eastern Alaska: A record of Eocene ridge subduction. *Geological*
950 *Society of America Bulletin*, 107(11), 1333-1355. [https://doi.org/10.1130/0016-](https://doi.org/10.1130/0016-7606(1995)107%3C1333:SHOTCM%3E2.3.CO;2)
951 [7606\(1995\)107%3C1333:SHOTCM%3E2.3.CO;2](https://doi.org/10.1130/0016-7606(1995)107%3C1333:SHOTCM%3E2.3.CO;2)
- 952 Peacock, S. M. (1987). Creation and preservation of subduction-related inverted metamorphic
953 gradients. *Journal of Geophysical Research: Solid Earth*, 92(B12), 12763-12781.
954 <https://doi.org/10.1029/JB092iB12p12763>
- 955 Penniston-Dorland, S. C., Kohn, M. J., & Manning, C. E. (2015). The global range of subduction
956 zone thermal structures from exhumed blueschists and eclogites: Rocks are hotter than
957 models. *Earth and Planetary Science Letters*, 428, 243-254.
958 <http://doi.org/10.1016/j.epsl.2015.07.031>
- 959 Phillips, B. A., Kerr, A. C., Mullen, E. K., & Weis, D. (2017). Oceanic mafic magmatism in the
960 Siletz terrane, NW North America: Fragments of an Eocene oceanic plateau? *Lithos*, 274-
961 275, 291-303. <https://doi.org/10.1016/j.lithos.2017.01.005>
- 962 Powell, R., & Holland, T. J. B. (2008). On thermobarometry. *Journal of Metamorphic Geology*,
963 26, 155-179. <https://doi.org/10.1111/j.1525-1314.2007.00756.x>

- 964 Rusmore, M. E. (1982). *Structure and petrology of pre-tertiary rocks near Port Renfrew,*
965 *Vancouver Island, British Columbia* (Master's thesis). Seattle, WA: University of
966 Washington.
- 967 Rusmore, M. E., & Cowan, D. S. (1985). Jurassic–Cretaceous rock units along the southern edge
968 of the Wrangellia terrane on Vancouver Island. *Canadian Journal of Earth Sciences,*
969 22(8), 1223-1232. <https://doi.org/10.1139/e85-124>
- 970 Sakaguchi, A. (1996). High paleogeothermal gradient with ridge subduction beneath the
971 Cretaceous Shimanto accretionary prism, southwest Japan. *Geology,* 24(9), 795-798.
972 [https://doi.org/10.1130/0091-7613\(1996\)024%3C0795:HPGWRS%3E2.3.CO;2](https://doi.org/10.1130/0091-7613(1996)024%3C0795:HPGWRS%3E2.3.CO;2)
- 973 Seyler, C. E., Kirkpatrick, J. D., Faber, C., Licht, A., Šilerová, D., Regalla, C. (2022). Major
974 element whole rock and mineral analyses and U-Pb detrital zircon analyses of schist and
975 metabasalt mylonites from the Leech River Shear Zone, Version 1.0. Interdisciplinary
976 Earth Data Alliance (IEDA). <https://doi.org/10.26022/IEDA/112312>
- 977 Shekut, S., & Licht, A. (2020). Late Middle Miocene Emergence of the Olympic Peninsula
978 Shown by Sedimentary Provenance. *Lithosphere,* 1-20.
979 <https://doi.org/10.2113/2020/7040598>
- 980 Simpson, R. W., & Cox, A. (1977). Paleomagnetic evidence for tectonic rotation of the Oregon
981 Coast Range. *Geology,* 5(10), 585-589. [https://doi.org/10.1130/0091-](https://doi.org/10.1130/0091-7613(1977)5<585:PEFTRO>2.0.CO;2)
982 [7613\(1977\)5<585:PEFTRO>2.0.CO;2](https://doi.org/10.1130/0091-7613(1977)5<585:PEFTRO>2.0.CO;2)
- 983 Sisson, V. B., Hollister, L. S., Onstott, T. C. (1989). Petrologic and age constraints on the origin
984 of a low-pressure/high-temperature metamorphic complex, southern Alaska. *Journal of*
985 *Geophysical Research: Solid Earth,* 94(B4), 4392-4410.
986 <https://doi.org/10.1029/JB094iB04p04392>
- 987 Sláma, J., Košler, J., Condon, D. J., Crowley, J. L., Gerdes, A., Hanchar, J. M., et al. (2008).
988 Plešovice zircon — A new natural reference material for U-Pb and Hf isotopic
989 microanalysis. *Chemical Geology,* 249(1-2), 1-35.
990 <https://doi.org/10.1016/j.chemgeo.2007.11.005>
- 991 Spear, F. S. (1981). An experimental study of hornblende stability and compositional variability
992 in amphibolite. *American Journal of Science,* 281(6), 697-734.
993 <https://doi.org/10.2475/ajs.281.6.697>

- 994 Spear, F. S. (1995). *Metamorphic Phase Equilibria and Pressure-Temperature-Time-Paths* (2nd
995 ed.). Washington, D.C.: Mineralogical Society of America.
- 996 Stewart, R. J., & Page, R. J. (1974). Zeolite Facies Metamorphism of the Late Cretaceous
997 Nanaimo Group, Vancouver Island and Gulf Islands, British Columbia. *Canadian*
998 *Journal of Earth Sciences*, *11*, 280-284. <https://doi.org/10.1139/e74-024>
- 999 Syracuse, E. M., van Keken, P. E., & Abers, G. A. (2010). The global range of subduction zone
1000 thermal models. *Physics of the Earth and Planetary Interiors*, *183*(1-2), 73-90.
1001 <https://doi.org/10.1016/j.pepi.2010.02.004>
- 1002 Tajčmanová, L., Connolly, J. A. D., & Cesare, B. (2009). A thermodynamic model for titanium
1003 and ferric iron solution in biotite. *Journal of Metamorphic Geology*, *27*(2), 153-165.
1004 <https://doi.org/10.1111/j.1525-1314.2009.00812.x>
- 1005 Timpa, S., Gillis, K. M., & Canil, D. (2005). Accretion-related metamorphism of the Metchosin
1006 Igneous Complex, southern Vancouver Island, British Columbia. *Canadian Journal of*
1007 *Earth Sciences*, *42*(8), 1467-1479. <https://doi.org/10.1139/e05-043>
- 1008 Tréhu, A. M., Asudeh, I., Brocher, T. M., Luetgert, J. H., Mooney, W. D., Nabelek, J. L., &
1009 Nakamura, Y. (1994). Crustal architecture of the Cascadia forearc. *Science*, *266*(5183),
1010 237-243. <https://doi.org/10.1126/science.266.5183.237>
- 1011 Ujiie, K. (2002). Evolution and kinematics of an ancient décollement zone, mélange in the
1012 Shimanto accretionary complex of Okinawa Island, Ryukyu Arc. *Journal of Structural*
1013 *Geology*, *24*(5), 937-952. [https://doi.org/10.1016/S0191-8141\(01\)00103-1](https://doi.org/10.1016/S0191-8141(01)00103-1)
- 1014 Wells, R., Bukry, D., Friedman, R., Pyle, D., Duncan, R., Haeussler, P., & Wooden, J. (2014).
1015 Geologic history of Siletzia, a large igneous province in the Oregon and Washington
1016 Coast Range: Correlation to the geomagnetic polarity time scale and implications for a
1017 long-lived Yellowstone hotspot. *Geosphere*, *10*(4), 692-719.
1018 <https://doi.org/10.1130/GES01018.1>
- 1019 Wells, R., Engebretson, D. C., Snively Jr., P. D., & Coe, R. S. (1984). Cenozoic plate motions
1020 and the volcano- tectonic evolution of western Oregon and Washington. *Tectonics*, *3*(2),
1021 275-294. <https://doi.org/10.1029/TC003i002p00275>
- 1022 White, R. W., Powell, R., Holland, T., & Worley, B. (2000). The effect of TiO₂ and Fe₂O₃ on
1023 metapelitic assemblages at greenschist and amphibolite facies conditions: mineral
1024 equilibria calculations in the system K₂O-FeO-MgO-Al₂O₃-SiO₂-H₂O-TiO₂-Fe₂O₃.

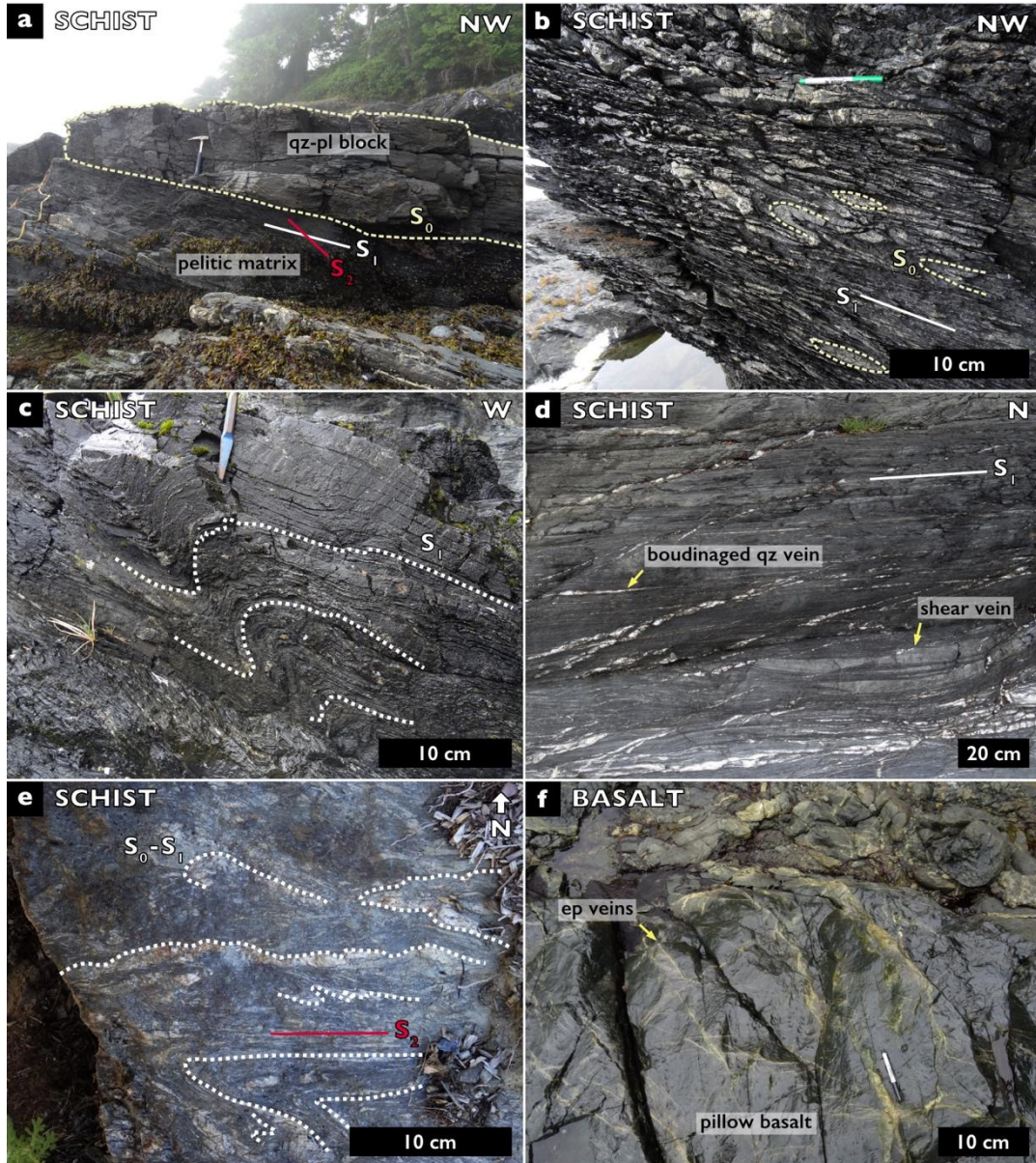
- 1025 *Journal of Metamorphic Geology*, 18(5), 497-511. <https://doi.org/10.1046/j.1525->
1026 1314.2000.00269.x
- 1027 Whitmeyer, S. J., & Karlstrom, K. E. (2007). Tectonic model for the Proterozoic growth of
1028 North America. *Geosphere*, 3(4), 220-259. <https://doi.org/10.1130/GES00055.1>
- 1029 Yorath, C. J., Sutherland Brown, A., & Massey, N. W. D. (1999). LITHOPROBE, southern
1030 Vancouver Island, British Columbia. *Geological Survey of Canada, Open File 498*.
1031 <https://doi.org/10.4095/210350>
- 1032 Zumsteg, C. L., Himmelberg, G. R., Karl, S. M., Haeussler, P. J., (2003). Metamorphism within
1033 the Chugach accretionary complex on southern Baranof Island, southeastern Alaska.
1034 *Special Papers-Geological Society of America*, 371, 253-267. <https://doi.org/10.1130/0->
1035 8137-2371-X.253



1036

1037 **Figure 1. Geologic map, cross-section, and structural data.** a) Simplified geologic map of
 1038 southern Vancouver Island (adapted from Cui et al., 2017; Groome et al., 2003; Muller, 1980;

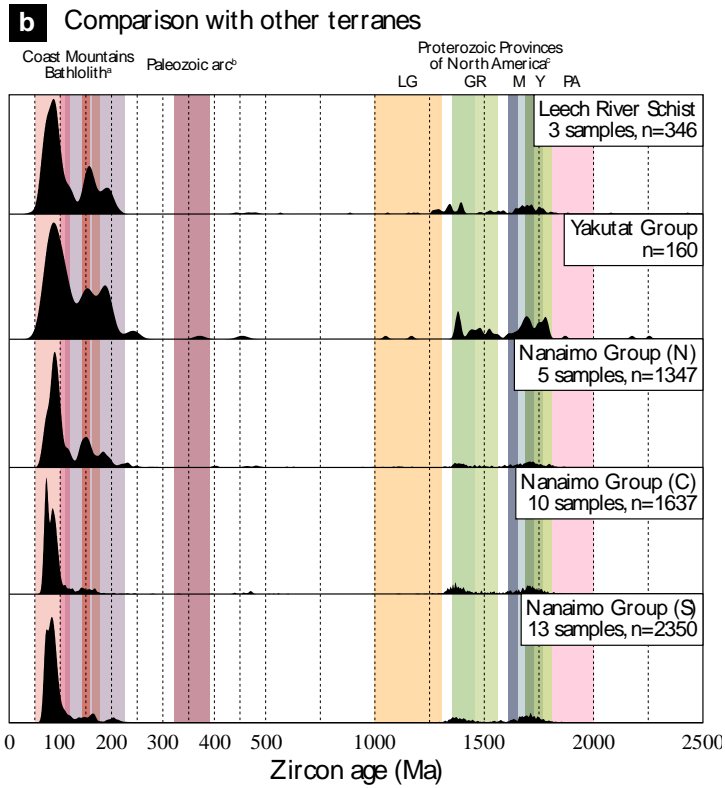
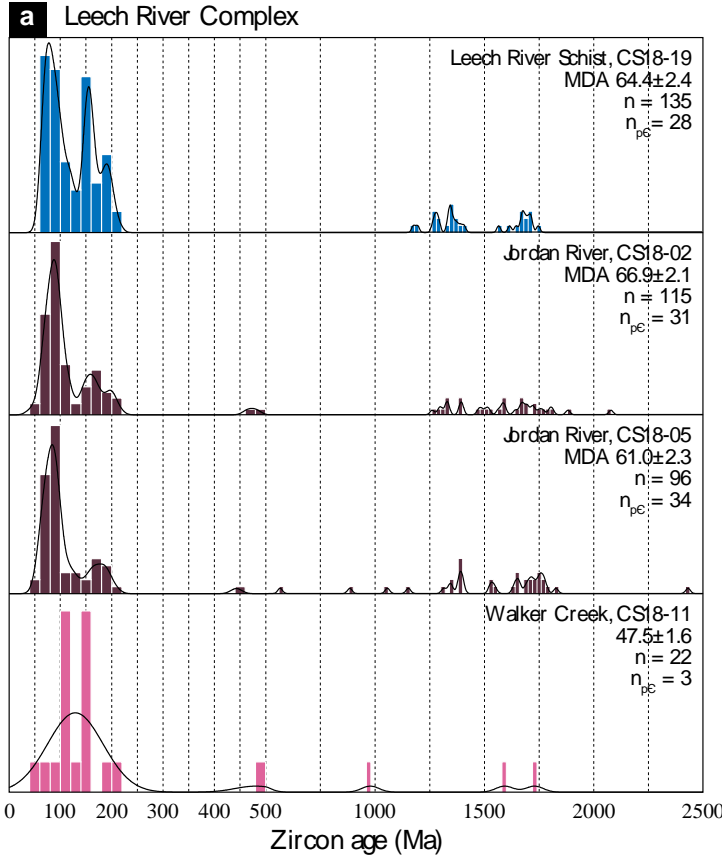
1039 Rusmore, 1982). Locations labelled with black arrows indicate field sites. Circles and triangles
1040 represent locations of samples collected for petrography and U-Pb zircon geochronology,
1041 respectively, with colors corresponding to the sampled units. LRSZ—Leech River Shear Zone;
1042 SJF—San Juan Fault; SMF—Survey Mountain Fault. **b)** Simplified geologic cross-section
1043 (adapted from Clowes et al., 1987; Hyndman et al., 1990). Stereonet projections of foliation,
1044 lineation, and fold orientations: **c)** Foliation, lineation, and fold orientations in the Leech River
1045 Schist near Botany Bay (~0.5 km² area); **d)** Foliation, lineation, and fold orientations within the
1046 Leech River Schist directly north of the Diversion and Bear Creek reservoirs (up to ~2 km north
1047 of the LRSZ); **e)** Foliation, lineation, and three sets of fold orientations within the Leech River
1048 Schist and Metchosin Basalt mylonites (~12 km along strike within the shear zone). Note that
1049 isoclinal folds with shallowly plunging hinges are underrepresented due to lack of subvertical
1050 exposures. Foliation planes and fold axial planes are plotted as poles to the planes. Structural
1051 field data can be obtained in Table S2.



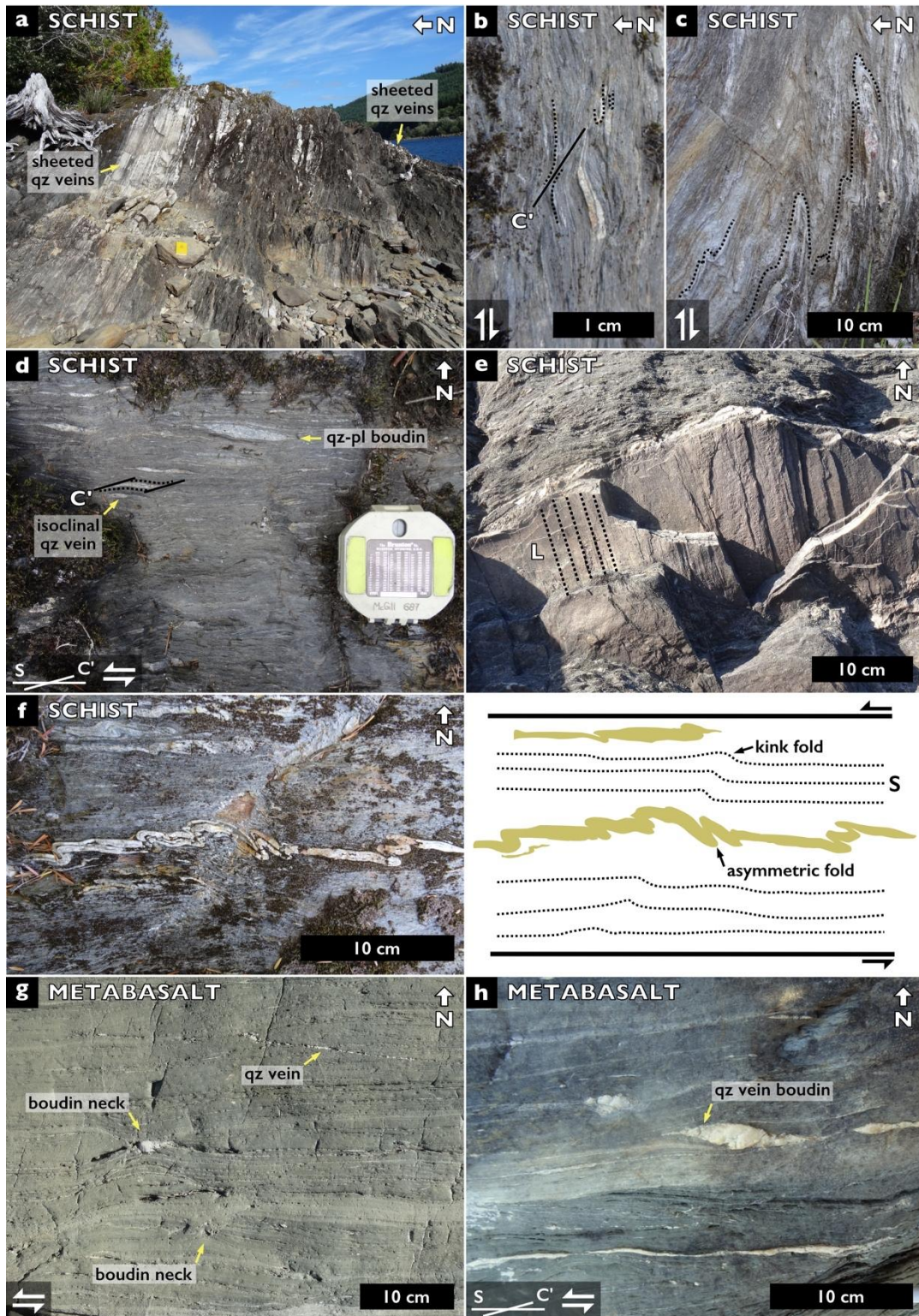
1052

1053 **Figure 2. Field photos of structures in the hanging wall and footwall.** Photos are from Botany
 1054 Bay (a-d), north of the Diversion and Bear Creek reservoirs (e), and Sombrio Point (f). **a**) Leech
 1055 River Schist at Botany Bay contains centimeter- to meter-scale quartz-plagioclase blocks within
 1056 a phyllosilicate-rich matrix, which defines a block-in-matrix texture and preserves original
 1057 bedding (S_0) between sandstone layers and shale. The matrix has two foliation orientations (S_1
 1058 and S_2), with S_1 subparallel to the long axes of blocks. **b**) Isoclinal folding of the S_{0-1} foliation
 1059 with subparallel axial planes. **c**) Asymmetric, disharmonic folding of the S_1 foliation with axial
 1060 planes subparallel to the S_2 foliation. **d**) Quartz veins within the LRS are oriented $0-30^\circ$ from the
 1061 S_1 foliation. Some shear veins host small amounts of displacement, while the veins subparallel to

1062 foliation are offset along S_1 . e) Leech River Schist directly north of the Diversion and Bear
1063 Creek reservoirs is composed of discontinuous quartz-plagioclase layers and micaceous layers.
1064 The S_0 - S_1 foliation is transposed into parallel with the dominant S_2 foliation and tightly folded
1065 into disharmonic and often asymmetric folds. f) Metchosin Basalt at Sombrio Point contains
1066 pillow basalts with abundant epidote veins.



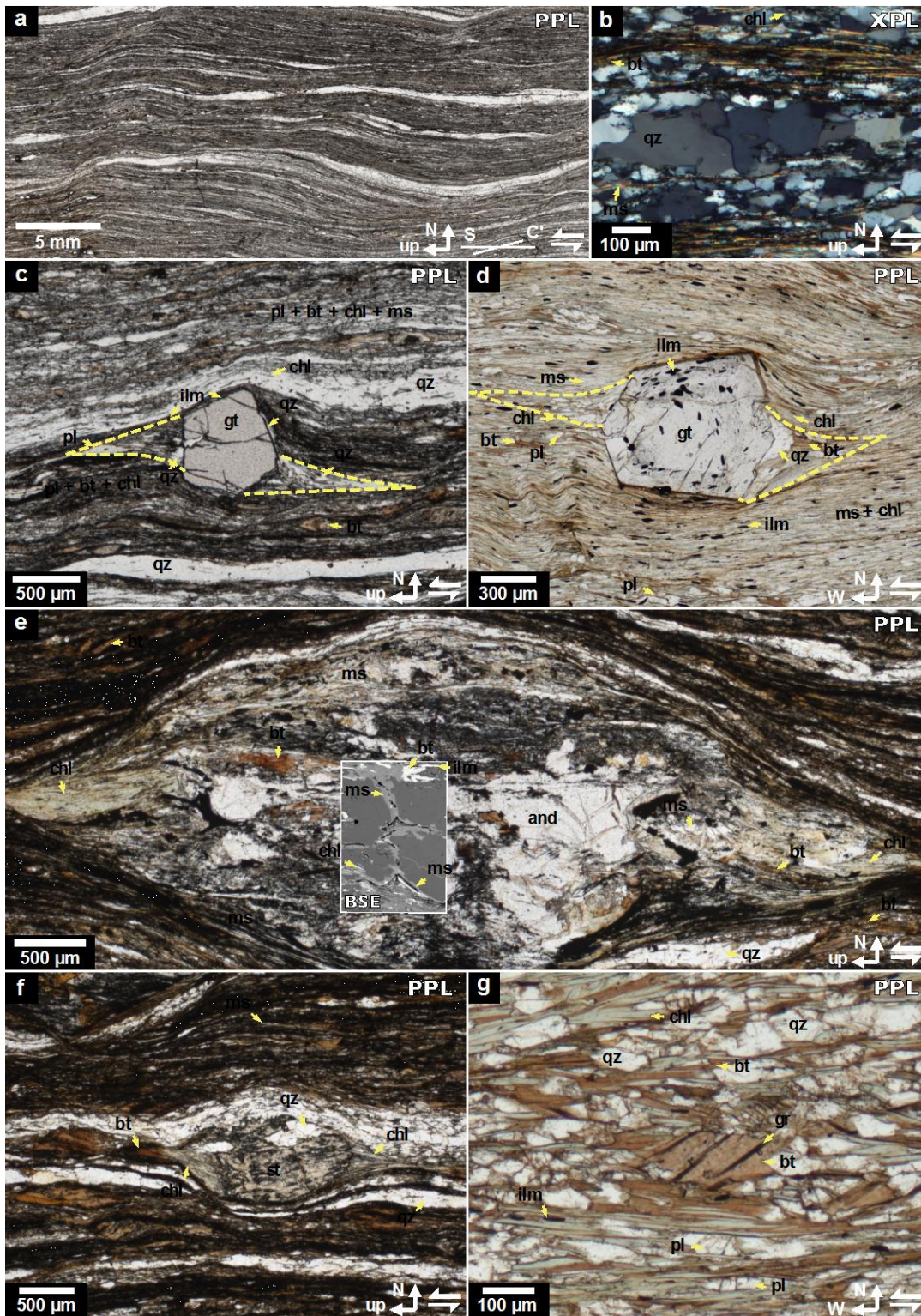
1068 **Figure 3. U-Pb detrital zircon geochronology of the Leech River Complex.** a) Histograms
1069 and kernel density estimates for detrital zircons from the Leech River Schist (CS1819, blue),
1070 Jordan River metasandstone (CS1802 and CS1805, purple), and the Walker Creek intrusions
1071 (CS1811, pink). Note that there is a break in scaling on the x-axis at 500 Ma, but the bin size is
1072 consistently 20 My. b) Detrital zircon age distributions (KDEs) from the Leech River Schist
1073 compared with the Yakutat Group (Garver & Davidson, 2015) and “Facies 2” zircons from the
1074 Upper Nanaimo Group (northern, central, and southern transects of Coutts et al., 2020; Englert et
1075 al., 2018; Matthews et al., 2017). Colored bars represent detrital zircon provenances from
1076 ^aGehrels et al. (2009), ^bNelson and Colpron (2007), and ^cWhitmeyer and Karlstrom (2007).
1077 LG—Llano-Grenville province. GR—Granite-Rhyolite province. M—Mazatzal province. Y—
1078 Yavapai province. PA—Paleoproterozoic arcs.



1079

1080 **Figure 4. Field photos of structure and kinematics of the mylonite zone.** Subvertical sections
 1081 contain north-side-up shear sense indicators and subhorizontal sections contain left-lateral shear
 1082 sense indicators. **a-c)** Subvertical sections of the Leech River Schist mylonite showing foliation

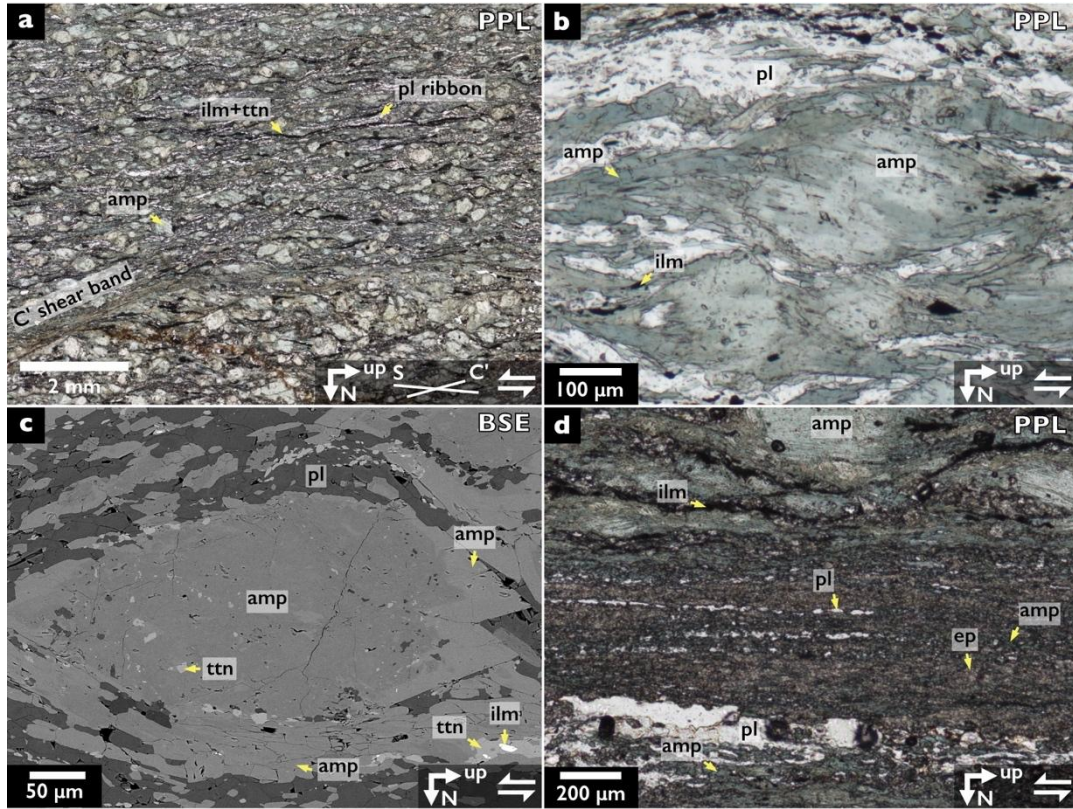
1083 defined by compositional layering and alignment of phyllosilicate basal planes, C' shear bands,
1084 isoclinal folding of quartz-dominated layers, and asymmetric folding of the foliation. **d)**
1085 Subhorizontal section of the LRS mylonite showing foliation, C' shear bands, boudinage of
1086 quartz- and plagioclase-dominated layers, and isoclinal folding of quartz-dominated layers. **e)**
1087 Steeply plunging stretching lineation (L) visible on foliation planes within the LRS mylonite is
1088 defined by aligned mineral aggregates of phyllosilicates. **f)** Subhorizontal section of the LRS
1089 mylonite showing asymmetric shear folding of a quartz- and plagioclase-dominated layer and
1090 kink folding of foliation (S). The schematic cartoon illustrates the two types of folds. **g-h)**
1091 Subhorizontal sections of Metchosin Basalt mylonite showing foliation defined by compositional
1092 layering, C' shear bands, and boudinage of compositional layering and quartz veins.



1093

1094 **Figure 5. Leech River Schist mylonite microstructure.** Photomicrographs in plane-polarized
 1095 (PPL) and cross-polarized (XPL) light. **a)** Foliation planes (S) defined by compositional layering
 1096 deflected by C' shear bands creating an asymmetric composite foliation. **b)** Quartz-dominated

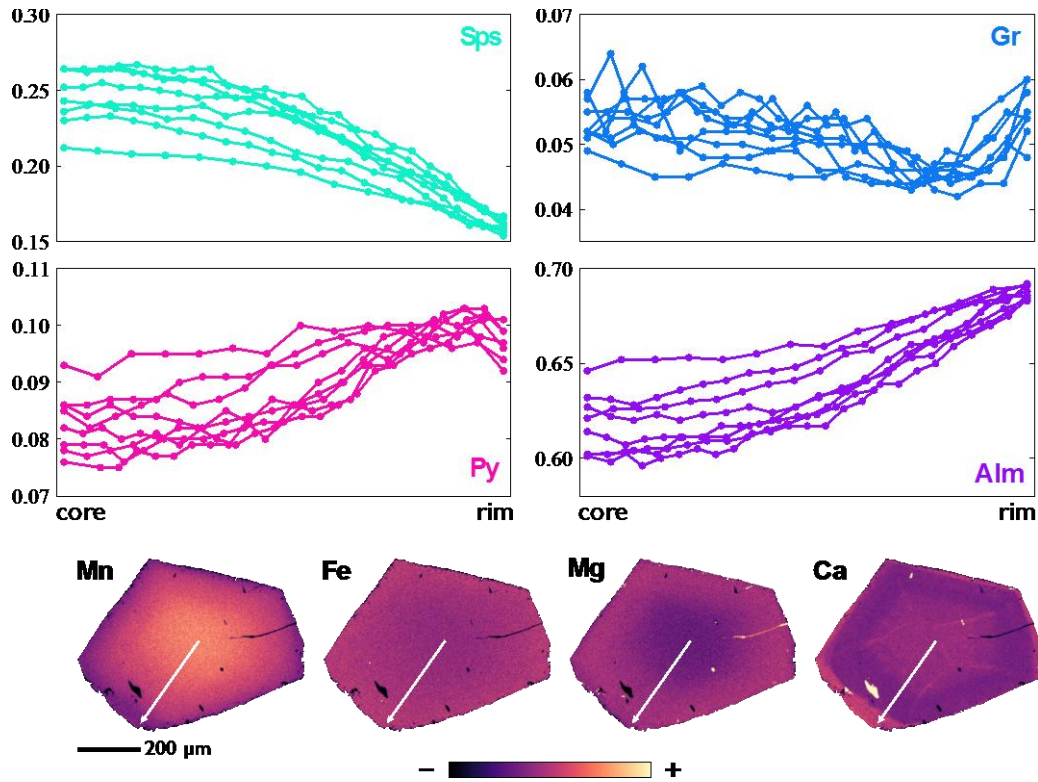
1097 layer with interlobate quartz grain boundaries. **c)** Garnet sigma-clast with asymmetric tails in
1098 lineation-parallel section. **d)** Garnet sigma-clast with asymmetric tails and rotated ilmenite
1099 inclusions in lineation-perpendicular section. **e)** Andalusite sigma-clast partially replaced by
1100 muscovite with asymmetric tails. **f)** Staurolite sigma-clast partially replaced by chlorite with
1101 asymmetric tails. **g)** Biotite porphyroblast with graphite inclusions and intergrown biotite and
1102 chlorite in a phyllosilicate-dominated layer. and—andalusite, bt—biotite, chl—chlorite, gr—
1103 graphite, gt—garnet, ilm—ilmenite, ms—muscovite, pl—plagioclase, qz—quartz, st—staurolite.



1104

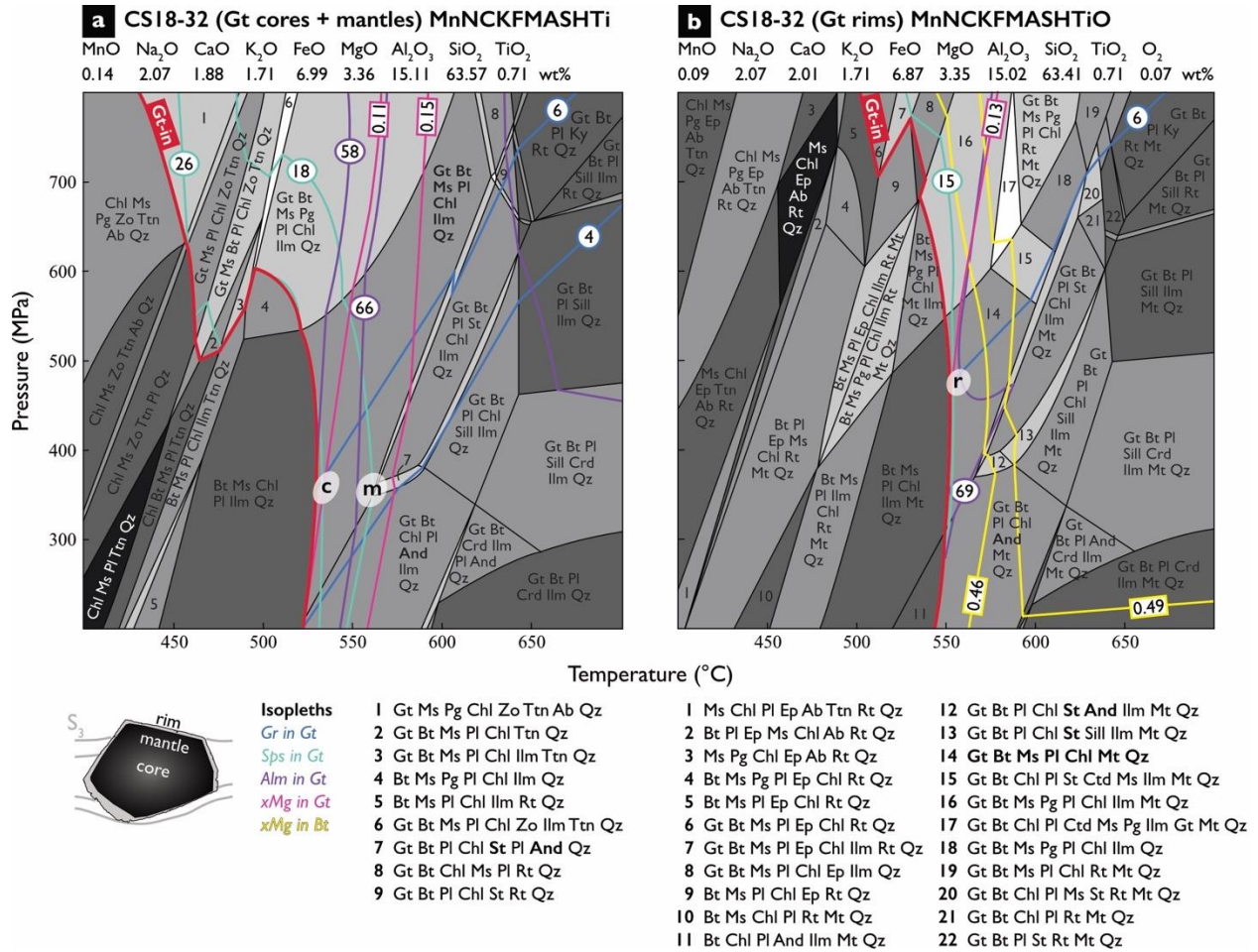
1105 **Figure 6. Metchosin Basalt mylonite microstructure.** Photomicrographs in plane-polarized
 1106 (PPL) and cross-polarized (XPL) light. **a)** Foliation planes (S) deflected by both C planes,
 1107 oriented horizontally, and C' shear bands creating an asymmetric composite foliation. **b-c)**
 1108 Chemical zoning between light green and dark green amphibole cores and tails. Fine-grained
 1109 plagioclase surrounding amphibole porphyroblasts. Ilmenite seams along edges of amphibole
 1110 domains. **d)** Fine-grained epidote-amphibole layer. amp—amphibole, ep—epidote, ilm—
 1111 ilmenite, pl—plagioclase, ttn—titanite.

1112



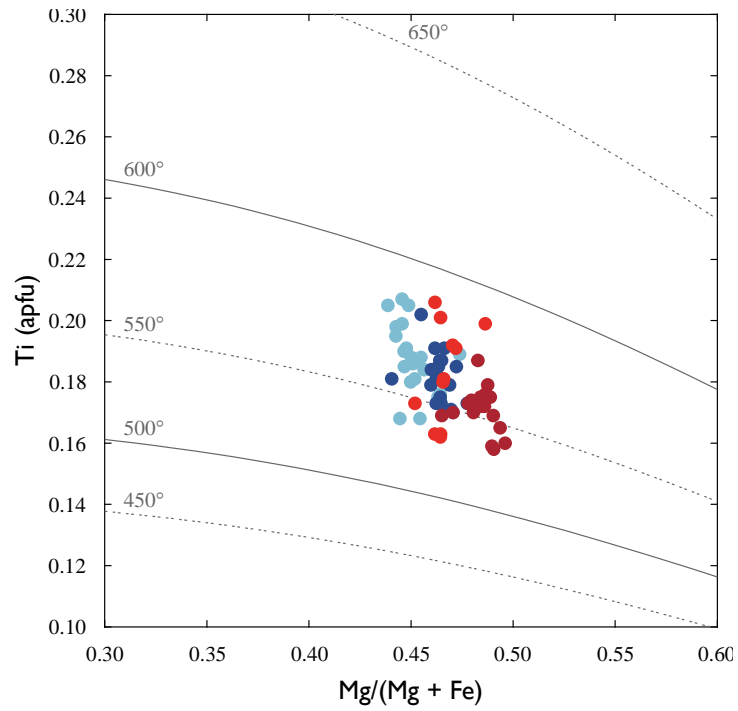
1113

1114 **Figure 7. Garnet compositions from the schist mylonite.** Garnet end-member fractions along
 1115 core-to-rim transects (**top**) and representative wavelength-dispersive X-ray spectroscopy (WDS)
 1116 maps (**bottom**) show garnet compositional zoning. In the cores and mantles, Mn and Ca content
 1117 decreases and Mg and Fe content increases during growth. Then, in the rims, Ca and Mg content
 1118 show a sharp change in thin, asymmetric rims. White arrows indicate location of microprobe
 1119 transect. Sps—spessartine (Mn); Py—pyrope (Mg); Alm—almandine (Fe); Gr—grossular (Ca).



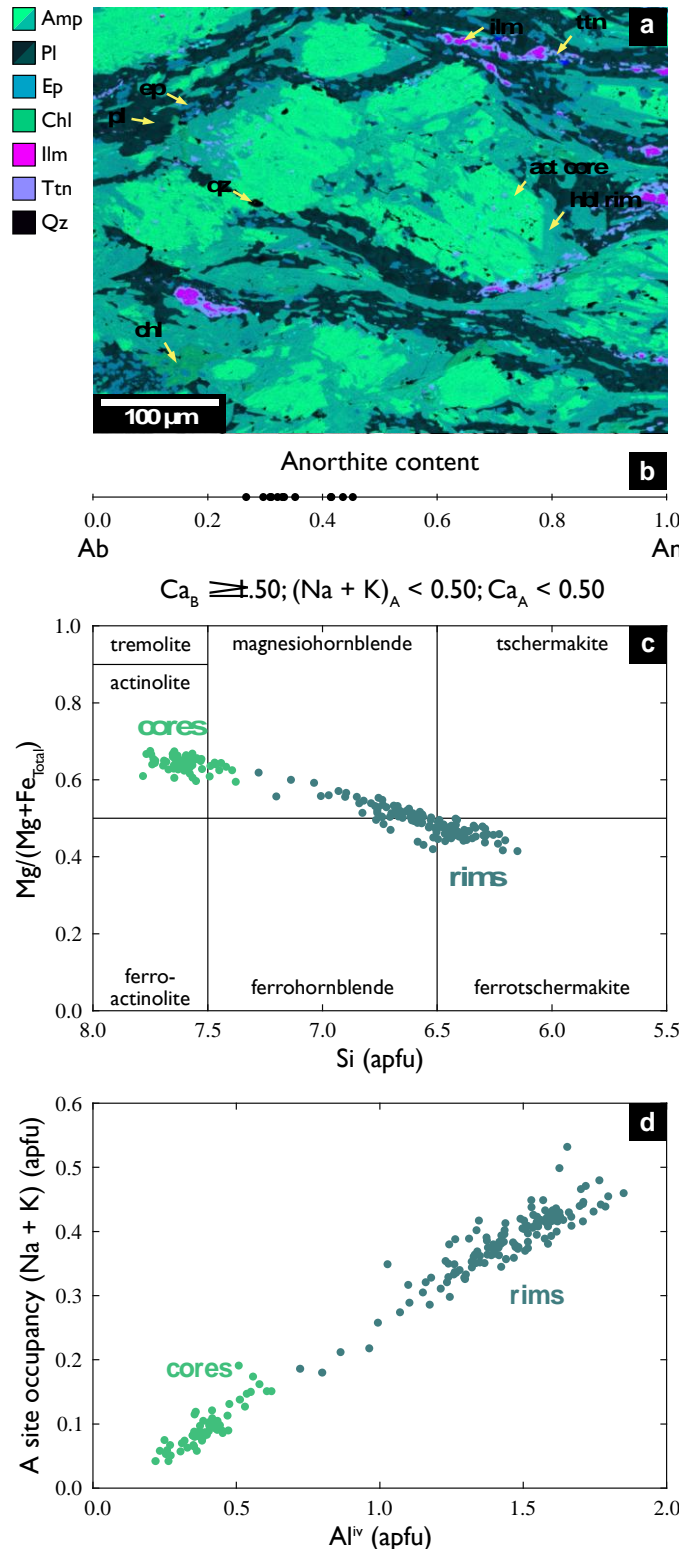
1120

1121 **Figure 8. P-T section for schist mylonite.** P-T sections generated for schist mylonite sample
1122 CS18-32 with contours of grossular (Gr), spessartine (Sps), and almandine (Alm) content as well
1123 as X_{Mg} for garnet core, mantle, and rim compositions. **a)** Garnet core compositions crossover at
1124 525–540 °C and 340–370 MPa, while mantle compositions crossover at 550–565 °C and 340–
1125 370 MPa. **b)** Garnet rim compositions crossover at 550–570 °C and 450–490 MPa. Garnet
1126 cartoon illustrating the mylonitic foliation orientation and compositional zoning that defines the
1127 cores, mantles, and rims. Ab—albite, And—andalusite, Bt—biotite, Chl—chlorite, Crd—
1128 cordierite, Ep—epidote, Gt—garnet, Ilm—ilmenite, Ky—kyanite, Mt—magnetite, Pg—
1129 paragonite, Pl—plagioclase, Qz—quartz, Rt—rutile, Sill—sillimanite, St—staurolite, and Ttn—
1130 titanite.



1131

1132 **Figure 9. Ti-in-biotite thermometry.** Ti content in biotite from the schist mylonite plotted on
1133 the Ti saturation surfaces of Henry et al. (2005). All analyses fall between the 500 and 600 °C
1134 contours.

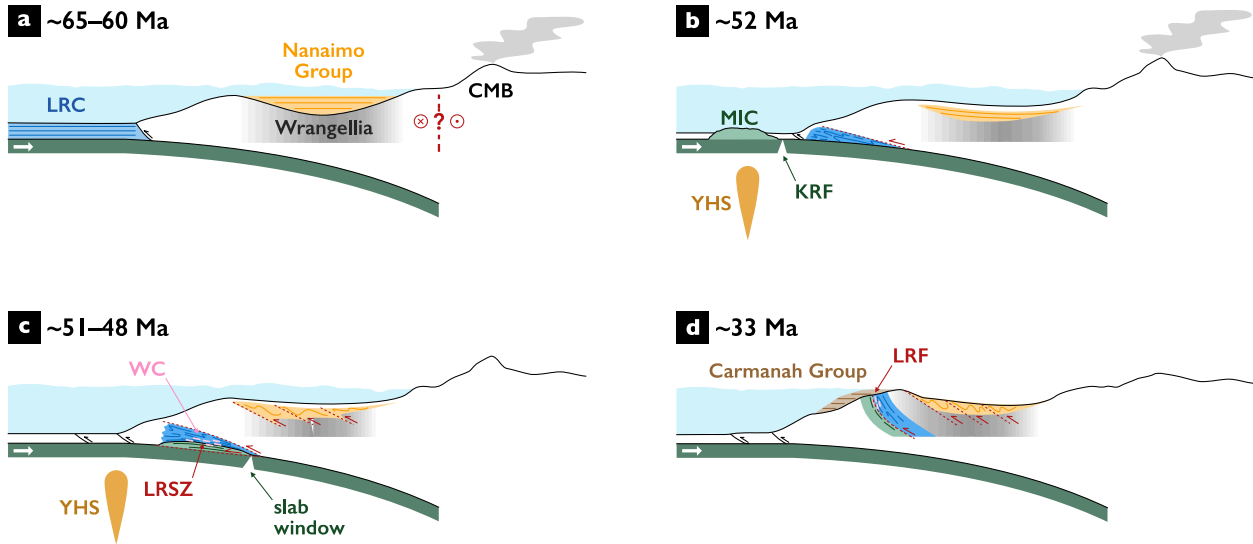


1135

1136 **Figure 10. Amphibole and plagioclase compositions from the metabasalt mylonite.**

1137 Chemical maps and point analyses from plagioclase grains and amphibole grains with chemically

1138 distinct cores and rims. **a)** False-colored phase map generated from multiple x-ray maps
1139 highlighting chemically distinct cores and rims. Rim compositions extend into syn-kinematic
1140 tails. **b)** Plagioclase compositions in the matrix range from An₂₇ to An₄₅. **c)** Amphibole core and
1141 rim compositions plotted onto a discrimination diagram with field labels following Leake et al.
1142 (1997). Cores primarily plot as actinolite, while rims plot as hornblende to tschermakite. **d)**
1143 Temperature-sensitive A site occupancy and pressure-sensitive tetrahedral alumina content
1144 demonstrate prograde growth of amphibole.



1145

1146 **Figure 11. Tectonic history of the LRC, MIC, and LRSZ.** Schematic cartoon (not to scale) of
 1147 the development of the Leech River Shear Zone and surrounding terranes from ~65 Ma to ~33
 1148 Ma. **a)** Synchronous deposition of the Leech River Complex and Nanaimo Group, possibly at
 1149 southern latitudes and followed by northward coast-wise translation. **b)** Formation of the MIC as
 1150 an oceanic plateau on the subducting oceanic plate near the Kula/Resurrection-Farallon ridge and
 1151 Yellowstone hotspot. Deformation of the LRC as part of the accretionary complex. Shallow
 1152 burial of the Nanaimo Group. Subduction of the Kula/Resurrection-Farallon ridge ahead of the
 1153 MIC. **c)** Deformation within the LRSZ accommodating subduction of the MIC beneath the LRC,
 1154 slab window formation and emplacement of the Walker Creek intrusions, and formation of the
 1155 Cowichan Fold-and-Thrust belt. **d)** Exhumation of the LRC and MIC to the surface where the
 1156 Oligocene-age Carmanah Group is uncomfortably deposited on top of the LRF in a coastal
 1157 marine environment. CMB—Coast Mountains Batholith. KRF—Kula/Resurrection-Farallon
 1158 ridge (slab window). LRC—Leech River Complex. LRF—Leech River Fault. LRSZ—Leech
 1159 River Shear Zone. MIC—Metchosin Igneous Complex. WC—Walker Creek intrusions. YHS—
 1160 Yellowstone Hotspot.